CENTRO DE INVESTIGACIONES EN ÓPTICA, A.C.

SPECTRAL AND TEMPORAL DYNAMICS IN ACTIVE Q-SWITCHED ERBIUM-DOPED FIBER LASERS

A THESIS SUBMITTED IN FULFILMENT OF THE REQUIREMENTS FOR THE DEGREE OF DOCTOR OF PHILOSOPHY IN THE FIELD OF SCIENCE (OPTICS)

Supervisors: Ph.D. Yury Barmenkov
Ph.D. Alexander Kiriyanov

Author: M.Ph. Josué Adin Minguela Gallardo

December 2017
León, Guanajuato, México

A Gaby y Zahra

Agradecimientos

Una tesis doctoral se construye en base a un enorme trabajo personal, pero detrás de cualquier investigación se esconde una sumatoria de esfuerzos colectivos que han permitido su realización. Antes de presentar el resultado de este trabajo de investigación, me parece justo recordar y agradecer el apoyo y la colaboración de todas aquellas personas que me han ayudado y que sin duda lo hicieron posible. Sin embargo, la lista es larga y escoger nombres para homenajear puede ser injusto, pero quiero agradecer con afecto a las siguientes personas:

A mis directores de tesis: Yuri Barmenkov y Alexander Kir'yanov *gracias* «**спасибо**» por sus oportunos consejos y las apropiadas directivas. También las acertadas recomendaciones críticas, siempre desde una perspectiva positiva y constructiva, que permitieron mejorase sustancialmente el trabajo.

Al Centro de Investigaciones en Óptica y al Consejo Nacional de Ciencia y Tecnología (CONACyT) por su apoyo financiero bajo el número de beca 252252, sin el cual no fuera posible dedicarle tiempo y esfuerzo a este trabajo doctoral.

Agradezco profundamente a mi esposa, Gabriela Alfaro Dardón quien me brindó su apoyo incondicional, me comprendió y tuvo tolerancia e infinita paciencia bajo cualquier circunstancia.

En particular a mis suegros y cuñados, quienes fueron padre y madre de Zahra durante días enteros, y han sido un pilar muy importante tanto de mi hija como de mi trabajo de tesis.

A mis padres y hermanos que son un pilar muy importante y por mostrarme su apoyo incondicional.

A Myriam Jiménez, técnico del Laboratorio de Fibras Ópticas, por su valiosa ayuda y soporte profesional.

A Mario Alberto Ruiz, por su ayuda profesional y profundas enseñanzas en el idioma inglés.

Al ingeniero Ricardo Valdivia por su soporte profesional.

A todos y cada uno de mis amigos del Doctorado y del Laboratorio de Fibras por su compañerismo y amistad que me ofrecieron.

A los investigadores que conformaron el sínodo para el examen doctoral, los doctores Miguel Ángel Bello, Olivier Pottiez, Alejandro Martínez e Ismael Torres, agradezco su tiempo y sugerencias aportadas a este trabajo de tesis. En particular agradezco al Dr. Olivier por su confianza depositada en mí al poder colaborar.

A mis amigos Mariana, Ernesto, Alberto, Javier y Enrique por sus valiosas sugerencias aportadas.

León, Gto., a 11 de diciembre de 2017

Abstract

In the present dissertation work, the spectral and temporal features of actively Q-switched erbium-doped fiber lasers are reported. These features were investigated for two common laser configurations: for the linear Fabry-Pérot cavity with a pair of fiber Bragg gratings as reflectors, and for one-directional ring cavity without spectrally selective elements. It is shown that in both configurations the spectral width of sub-pulses, forming a Q-switch pulse, depends on the sub-pulse number, the spectrum of the most powerful sub-pulse is much broader than those of the rest, less powerful ones. In the case of the ring laser, the optical spectra of sub-pulses shift to the Stokes side while increasing a sub-pulse's number. Possible reasons for such laser spectral dynamics will be discussed.

We also report properties of the intensity noise of actively Q-switched erbium-doped fiber lasers implemented in these two configurations. We demonstrate that the types of photon noise statistics of Q-switched pulses in these two lasers are dramatically different (Poissonian or Bose-Einstein), revealing a crucial role of the cavity's spectral selectivity. To determine the type of experimental statistics in terms of photon noise distribution, a detailed modeling is performed. Finally, the noisy Q-switched pulses are employed as a pump for generating broadband supercontinuum in telecom fiber, which affects their noise statistics.

Keywords: Erbium-doped fiber laser, active Q-switching, temporal dynamics, spectral dynamics, laser noise, photon statistics, nonlinear effects, supercontinuum generation.

Contents

List of Figures

Chapter 1 Introduction

Rare-earth doped fiber lasers have attracted increasing attention recently in many fields, such as laser machining, telecommunications, and medicine, because of their excellent beam quality, high brightness, outstanding efficiency, diverse wavelength selection and good compactness [1], [2]. For many applications, such as laser marking, engraving and machining, optical time domain reflectometry (OTDR) and laser ranging, lasers with high intensity and short pulses are required [3].

Q-switch is an effective method to obtain giant short pulses from a laser [3], [4]. In a Q-switching operation, the cavity loss is kept at a high level until the pumped gain medium has stored a certain amount of energy. The cavity loss is then quickly reduced to a small value, which allows the intense stimulated laser radiation to establish quickly in the cavity. A short optical pulse is finally released, and its energy can be in the microjoule to joule range [3], [4].

Q-switching can be realized in either an active or passive way. The former usually needs an active control element, e.g., either an acousto-optic modulator (AOM), an electro-optic modulator (EOM), or a mechanical element (such as a rotating mirror). In contrast, a saturable absorber is usually adopted in a passive Q switch. In both types of Q-switch lasers, the pulse duration is in the nanosecond range (corresponding to several photon round-trips along a cavity), and the pulse repetition rate is usually in the range from a few Hertz (namely *Pulse on Demand*) to hundreds of Kilohertz [5].

With further investigation of the mechanism of the multi-peak phenomenon, usually observed in Q-switched pulses (sometimes called “Q-switching with self-mode-locking” [6]), it was understood the switching dynamics that was considered in the traditional Q-switching theory, especially in the theory of fiber lasers with long cavity and high gain [7], [8]. It has been shown that the giant pulses generated by actively Q-switched fiber lasers are composed of a train of sub-pulses spaced by the photon round-trip time in the laser cavity. Pulses of such type are usual for erbium-doped FLs (EDFLs) assembled in both common Fabry-Perot (F-P) and ring geometries [9]–[12]. Generation of multi-peak or split Q-switched pulses have been widely reported, both experimentally and theoretically, for yt-

terbium [13], neodymium [14], thulium [15], holmium [16], and, of course, for erbium [8] doped fiber lasers. Indeed, the mechanisms that lead to such behavior of the Q-switch pulse is related to a saturation energy of active fiber, amplified spontaneous emission (ASE), excited-state absorption, if present, passive intra-cavity loss, and relatively long laser cavity [17].

1.1 Motivation

AQS FLs are well described by the traveling waves' model where the laser is considered as a multi-pass amplifier of spontaneous emission (SE), several times reflected by narrowband fiber Bragg gratings (FBGs) in the case of an F-P cavity is used [8], [13]. A similar model may be applied to active Q-switched fiber lasers (AQS FLs) with a ring cavity, but in this case one needs to account for the spectral variations of the active fiber's gain, given that each sub-pulse in the train affects population inversion of an active fiber [1, Ch. 5]. However, no experimental evidence has been performed before our present work of such spectral variation for ring AQS FL to the best of our knowledge.

Additionally, since Q-switched pulse waveform oscillates in the range of nanoseconds, the pulse characterization in time-domain have commonly been made by photodetectors and oscilloscopes with relatively low radiofrequency (RF) bandwidth, in the range of 100 MHz to 500 MHz. However, when fast electronics is employed (with bandwidth near to the optical bandwidth), the pulse-to-pulse jitter and high amplitude variations become more evident, see, for example, the pulse fluctuation in [18]. The origins of these effects have been attributed to random fluctuations in the gain built up time. However, a deep study of such fluctuations is required.

The principal aim of this dissertation work is to investigate the rich dynamics of AQS pulsing observed in FLs in both spectral and temporal domains. This study is interesting and significant for understanding the physics behind Q-switching phenomenon in fiber lasers, especially, when Q-switched pulses from FLs with different types of cavities, such as the F-P (optically narrowband lasing) and the ring (optically broadband lasing) cavities, are compared.

1.2 Outline of the Thesis

This thesis develops the content of the peer-reviewed Papers I and II reproduced at the end of the thesis. In the course of this work, AQS pulses from FLs with two different cavity configurations

were studied and evaluated experimentally, focusing on AQS erbium-doped fiber lasers (AQS EDFL). The experimental evaluation had three desired objectives: 1) to understand the spectral dynamics, 2) to understand the temporal (noise) dynamics of pulsing from AQS EDFL, and 3) to compare these dynamics for AQS FLs with cavities based on optically filtered and non-filtered feed-backs.

In Chapter 2 the basic description of the erbium ion embedded into a silica matrix and theoretical overview of FLs with two mostly utilized F-P and ring cavities and theirs' temporal and spectral dynamics under AOM switching ON action are discussed. This chapter also provides a review of the literature in relevant numerical models that helps one to understand the physics behind pulsing in AQS EDFLs. At the end of Chapter 2, the Bose-Einstein and the Poison statistics are reviewed for the case when they are applied to amplified spontaneous emission playing the key role of a seed source for AQS pulses.

Chapter 3 is focused on describing the results of Paper I in which erbium-based AQS FLs with F-P and ring cavities are developed. First, the experimental arrangements of both types of FLs used in the experiments are discussed in details. Then, the experimental results describing dynamics of the AQS pulsing and also variations in the optical spectrum with the AOM repetition frequency change are presented. Finally, the dynamics of optical spectra measured separately for each sub-pulse of which the AQS pulses consist is discussed, providing at the same time a quantitative model for the optical spectrum dynamics.

Chapter 4 provides details of the results discussed in Paper II in which the temporal behavior of AQS pulsing of lasers based on F-P and ring configurations are reported. The main topic discussed here is a statistical characterization of the intensity noise observed in the pulses from AQS EDFLs arranged in the two mentioned-above configurations. Detailed modeling of the photon noise distribution is also performed.

Particularly, AQS pulses and their noise statistics were studied and compared before and after propagating along 100-m long SMF-28 communication fiber, mainly for clarification of the factors that affect the photon statistics, and to establish a relationship between temporal and spectral characteristics of the pulse after its spectral broadening due to nonlinear optical effects arising in the fiber under high power noise.

In Chapter 5 the influence of nonlinear processes behind supercontinuum (SC) generation in AQS EDFL are discussed, with emphasis on SC-induced modifications observed in the temporal domain, particularly in the photon noise distribution.

Chapter 6 is the final chapter of this dissertation work. It provides a summary of the results presented in each chapter and states the overall conclusions.

Chapter 2 Background

In this chapter, a brief introduction of spectral and temporal properties of erbium-doped fibers (EDFs) and AQS is presented. First, the optical and electronic properties of the Er^{3+} ions in a silica host are reviewed in Section 2.1; then dynamics of AQS EDFL is discussed in Section 2.2, including FLs based on linear F-P (subsection 2.2.1) and ring (subsection 2.2.2) cavities. After that, a modeling AQS EDFL based on two contra-propagating laser waves and distributed laser amplifier is presented in details in subsection 2.2.3, which confirms our experimental results regarding the temporal evolution of AQS pulses. Finally, the quantum statistics of spontaneous emission is discussed in Section 2.3 for its posterior application in the study of the noise properties of AQS pulses in real AQS EDFLs' schemes under the scope of this dissertation work.

2.1 Introduction to the Erbium-Doped Fiber

The optical properties of Er^{3+}-ions embedded to silica host, which are quite relevant for AQS fiber lasers, are determined by the energy levels of the 4f electrons. Figure 1 shows these energy levels and the sublevels attributable to Stark splitting for Er^{3+}-ions in silica glass. The decay of the $^4I_{13/2}$ level is essentially radiative, because of the extremely low non-radiative decay rate. In combination with the low radiative transition rate, this decay results in an extremely long lifetime of about 10 ms for this energy level, which highly favors population inversion and therefore optical gain between the $^4I_{13/2}$ excited level and the $^4I_{15/2}$ ground state [19].

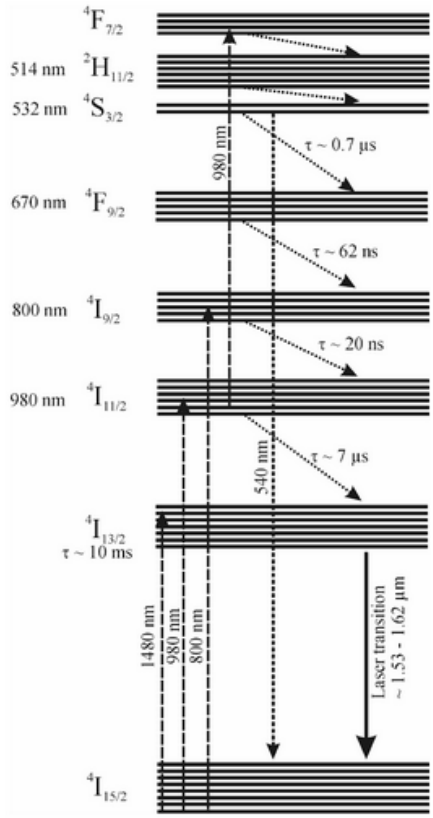

Figure 1. Er^{3+}-energy levels structure. Some of the pump excited state and the fluorescence transitions are indicated by dashed arrows, while the laser transition is shown by solid arrow. Diagonal dashed arrows indicate non-radiative transitions. At the left, the transitions wavelengths from the ground state to various energy levels are mentioned in nanometers. Adapted from [20].

Many transitions can be principally used for pumping of the Er^{3+}-ions. However, 980 nm and 1480 nm are the preferred pump wavelengths, mostly due to the availability of high power laser diodes and the relatively high absorption cross-sections of the Er^{3+}-ions at these wavelengths. The 980 nm pump transition terminates in the $^4I_{11/2}$ level, while for the 1480 nm transition the upper pump and the upper laser level lay within the same band. Thus, the main advantage of the 1480 nm pump band is a low quantum defect between pump and signal photons, which ensures a high laser efficiency. Furthermore, a visible side effect of the 980 nm pump wavelength is a green fluorescence of the erbium-doped fiber. This effect have been attributed to excited state absorption (ESA) from the upper pump level and subsequent phonon (mostly) and photon (in a small part) relaxation from the $^2S_{3/2}$ level and can be as high as 35% of the pump loss, resulting in a detriment of the Q-switch output power [17]. However, as it have been shown in [18], for 1480 nm pumping, the pump ESA is smaller, increasing, therefore, the Q-switch laser performance.

The erbium fiber lasers and amplifiers are generally based on a simplified few-level energy scheme, with the 1.55 µm emission arising from the $^4I_{13/2} \rightarrow {}^4I_{15/2}$ transition. The value of the emission cross-section of this transition and the shape of their spectra are host dependent and should be determined experimentally to model fiber lasers or amplifiers, which is important for optimization of their parameters.

Typical absorption and emission curves of a standard erbium fiber based on a silica glass are given in Figure 2. These curves show the normalized absorption and emission spectra obtained for EDF fabricated by Liekki/nLight. The fiber was obtained by using the so-called Direct Nanoparticle Deposition (DND) Technique [21] that provides independent control of the composition of hundreds of doped layers that make up the core without additional overcladding [22], thereby allowing precision, accuracy, and uniformity in the index and rare-earth-dopant profiles, which is important for producing fibers well suited for power scaling. (Note that the erbium-doped fiber used in our experiments is fabricated by Liekki/nLight using DND Technique.)

Additionally to the emission and absorption cross-sections for the pump and laser transitions, for modeling one needs to measure the fiber saturation intensity over the optical pump power [19], [23], as well as relaxation times of the laser and other levels, partial weights of pairs and clusters of the active ions if the fiber is highly doped, *etc.*; but experimental study of the active fiber parameters is beyond the scope of this dissertation work. It is relevant to note that in our experiments we implement the 1480 nm pump laser diodes to diminish the pump ESA in relatively high-doped Erbium fiber.

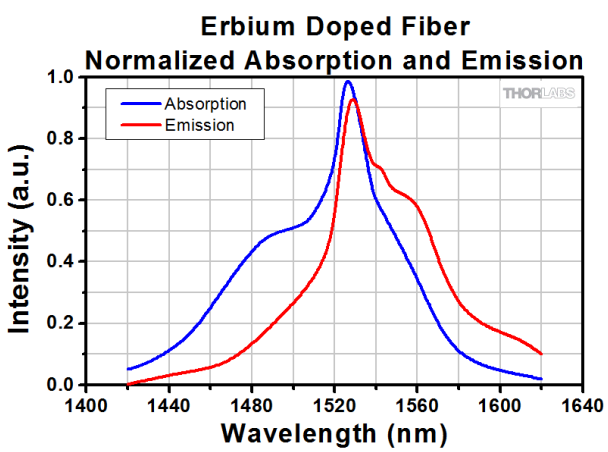

Figure 2. Normalized emission and absorption spectra for erbium-doped fiber fabricated by Liekki using the DND method (figure from Thorlabs.com).

When 1480 nm pump is used, Er^{3+} can be simplified from the 3-level to the two-energy level system [1], and the populations at the levels different from the ground and the laser ones can be omitted; hence, the sum of populations of these two levels is assumed to be a constant, and equal to the erbium ions concentration.

2.2 Switching Dynamics

Q-switched fiber lasers exhibit different features, and some of their temporal and spectral properties influencing on Q-switched pulsing depend dramatically on the cavity geometry. Therefore, a thorough understanding of these issues is important. In this section, we provide a comprehensive analysis of the switching dynamics of actively Q-switched fiber lasers with F-P and ring cavities for different cavity length and switching conditions.

When the rise time of an AOM, used for modulating Q-factor in laser cavity, is short while the cavity length is long, the actively Q-switched (AQS) pulses consist of a train of sub-pulses (ripples) separated by a time interval equal to the photon round-trip in the cavity. The occurrence of the multi-peak phenomenon is not determined by factors such as dopant type, single-clad or double-clad fiber, modulator type (AOM or electro-optic modulator), or the cavity type [13]. In fact, there are two types of fiber laser cavity structures that have been used extensively; one of them is the F-P (linear) cavity shown in Figure 3, in which the selective mirrors based on fiber Bragg gratings (FBGs) are usually used as the cavity couplers for two contra-propagating laser waves, and the other is the ring cavity (shown below in Figure 9). In contrast with the linear cavity, in the ring cavity, a unidirectional propagation of the laser wave is usually used, which is achieved by using an isolator that renders the internal field in the form of traveling wave in either counter-clockwise (CCW) or clockwise direction (CLW). These two types of cavities can be modeled with the traveling-wave model [8], [24] but with different boundary conditions. Particularly in a linear cavity, at either fiber end, a portion of the output light will be reflected back and re-injected into the same fiber end. Whereas, in a ring cavity, the output light leaving from one fiber end will be injected into the opposite fiber end. Therefore, different dynamic characteristics are expected due to such difference in the laser wave coupling.

The linear and ring cavities will be discussed below in subsection 2.2.1 and in subsection 2.2.3; the traveling-wave model will be briefly exposed too. Even though, the modeling of Q-switch lasers is far from the scope of this thesis.

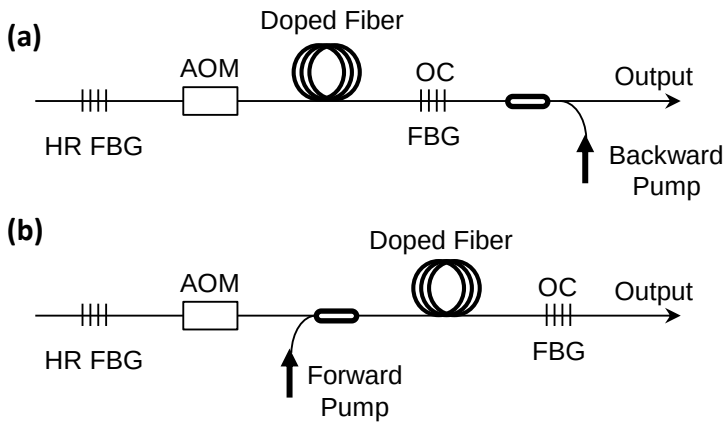

Figure 3. Configurations of actively Q-switched fiber lasers under (a) backward pump and (b) forward pump. AOM: acousto-optic modulator; FBG: fiber Bragg grating; HR: high-reflection; OC: output coupler.

2.2.1 AQS EDFL with linear F-P cavity

We consider the forward and backward pumped configurations shown in Figure 3. Both the backward (Figure 3 (a)) and the forward (Figure 3 (b)) pump waves are coupled through fused fiber couplers. In fact, other pumping techniques using end pumping through dichroic mirrors [25], side pimping via V-grooves [26] or a prism [27] can be applied to these configurations. A major difference between forward and backward pumping consists in distinct locations of the pump coupler that can lead to unavoidable attenuation of the pump wave, and different inversion distributions that can impact the signal amplification in EDF. In our experiments, the backward pumping configuration was chosen to separate the pump wave at the laser output on the left side of the wavelength division multiplexer (WDM), see Figure 4.

Fiber Bragg grating (FBG) based Q-switched fiber laser is attractive due to its superior all-fiber structure, low loss, good repeatability, and low cost [28]. FBGs are used in the following manner: a high-reflection FBG is used as the rear coupler of the laser cavity, which reflects up to 100% of the laser signal at the selected wavelength (Bragg wavelength) back to the active fiber, and a low-reflection FBG (usually with reflectivity in the range from $\sim 7\%$ to $\sim 30\%$) is used as the output coupler.

It is known that the exact temporal evolution of the pulse built-up is determined by many factors, such as the cavity length, waveguide parameters of the active fiber, intra- and extra-cavity losses, lasing and pumping wavelengths, pump power, pumping method, and dopant concentration. Additionally, the pulse built-up is related to the switching process of the AOM, such as the rise and opening times, switching function. In the following discussion, we will focus on two domains of the AQS laser dynamics: (a) the temporal domain and (b) the spectral domain.

A typical backward pumped F-P FBG-based cavity is shown in Figure 4. The operation principle is fully described by the model of two contra-propagating laser waves in F-P cavity, once considering the laser as a multi-pass amplifier of spontaneous emission reflected several times by selective mirrors (FBGs) [7], [8]. The process of a Q-switched (QS) pulse formation may be described as follows. When a step voltage is biased to the AOM's driver, the AOM gets rapidly opened (during ~ 50 ns, see Figure 5 (a)). At this moment ASE propagating in the right direction (see Figure 4) begins to pass through AOM with simultaneous frequency shift equals to the AOM operation frequency (110 MHz in our case). Then, part of the whole ASE power is reflected by FBG2, forming a seed signal that passes through AOM but in the left direction. After that, the seed wave is amplified in the active fiber and then is reflected by FBG1, and so on. Note that the total frequency shift of the laser wave is 220 MHz per round-trip.

The drown scenario explains the origin of sub-pulses as they appear in Figure 5 (b) at the different AOM's repetition rates. Notice that each subsequent sub-pulse appears at the laser output after the next round-trip through the cavity. After a few travels through the cavity, a pulse in the form of such sub-pulses reaches enough power to depopulate Er^{3+} laser level in EDF, which therefore limits their number. It also deserves mentioning that each sub-pulse is characterized by a sharp increase of optical power on its leading edge (which depends on AOM's rise time) and by an exponential fade on its trailing edge (which is explained by the gradual depopulation of Er^{3+} laser level due to amplification). For higher frequencies, the AQS pulse envelope becomes lower and wider (see Figure 5 (b)) and drift to longer times.

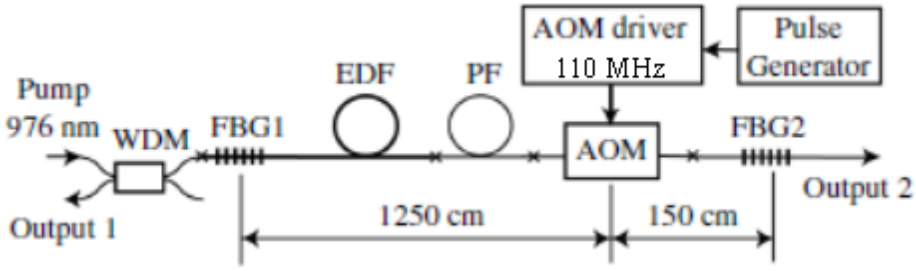

Figure 4. Backward pumped F-P cavity. Adapted from [11].

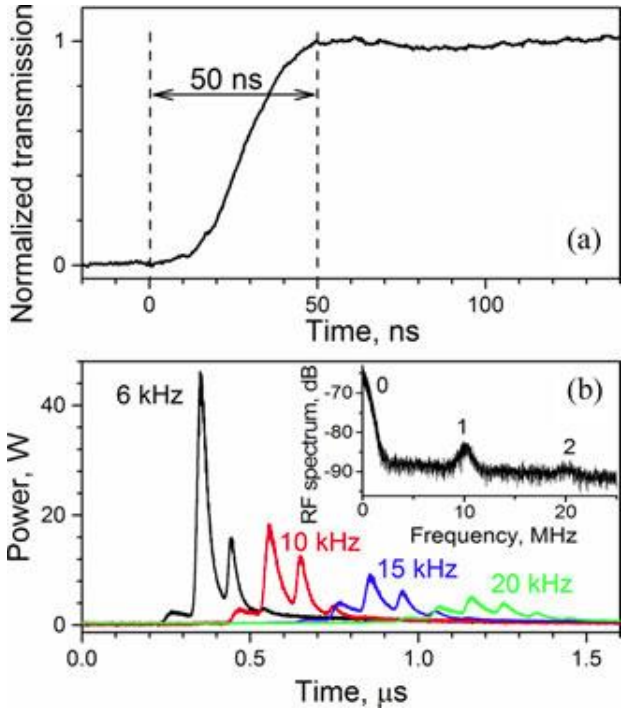

Figure 5. (a) AOM's transmission after its switching ON. (b) AQS pulses measured at some AOM repetition frequencies (AOM gate is always 2 µs). Zero-time in both snapshots corresponds to the moment when AOM gets opened. Adapted from [11].

Temporal Characteristics

An important fact observed in time domain is that in literature the pulse waveforms are reported after averaging by tens to hundreds of realizations mostly due to laser noise and also timing jitter. One of the first explanations of the amplitude fluctuations was associated with thermal effects inside the AOM device [29]. Recently two experiments were carried out using the same cavity configuration but with different effective radio-frequency (RF) bandwidths of the receiving devices (see Figure 6), at the left with an effective RF bandwidth (EBW) of 125 MHz [30], and at the right with EBW of 2.5 GHz [18]. The jitter and high amplitude noise apparently arise when the bandwidth of the detection sys-

tem (photodetector-oscilloscope) is higher than 1 GHz. Kolpakov *et al*. attributed the variations in amplitude and timing jitter to variations in inversion population from pulse to pulse [18].

Hence, the source of the noise is still not quite clear, and any detailed description of its study has not been reported so far.

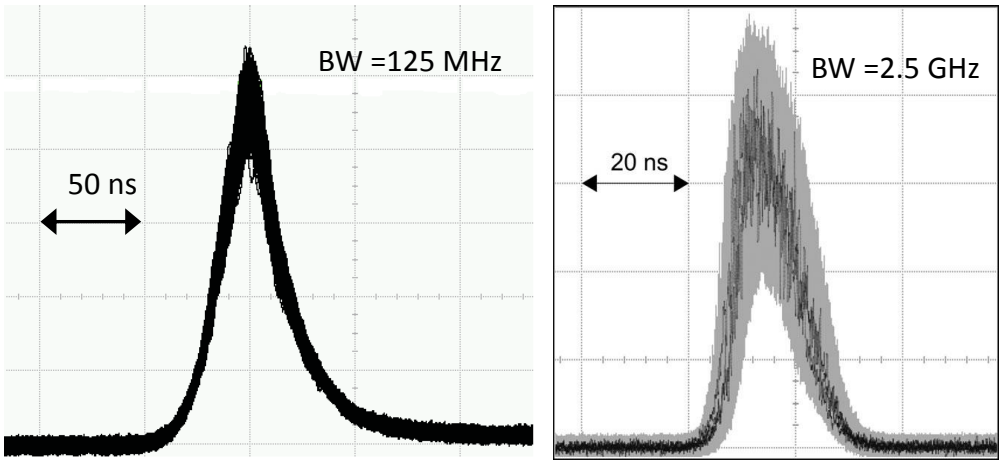

Figure 6. Infinite persistent figure shows the jitter and amplitude variation depending on the detection bandwidth. (a) Detection bandwidth is 125 MHz. Adapted from [30]. (b) Detection bandwidth is 2.5 GHz. Adapted from [18].

Spectral characteristics

In Q-switched fiber lasers, since the most attention is normally paid to the temporal dynamics, the spectral characteristics usually are not studied, due to its relatively weak influence [1] when the laser power is low. Here, the optical spectrum of the QS pulses from FL assembled in F-P configuration repeats the composed FBG's reflection spectra, i.e., equals to the product of both FBG's reflection spectra. As an example, from Figure 7 one can compare the spectra of AQS pulses with one of the output laser grating (FBG1): spectrum of FBG1 fits one of AQS pulse quite well. However, a fit by the product of the spectra of FBG1 and FBG2 is not shown.

It is worth mention that at each reflection of the laser wave by FBGs, spectra of sub-pulses becomes narrow as the sub-pulse number increases [8]; however, existing optical spectrum analyzers can measure only the spectra averaged over relatively long integration time of the internal photodetector and so it is not possible to get spectra of only a part of the whole AQS pulse. Due to such limitations in operation principle of optical spectrum analyzers, the spectral dynamics of pulses from AQS FLs with any geometries of the laser cavity, including F-P and ring ones, has never been studied.

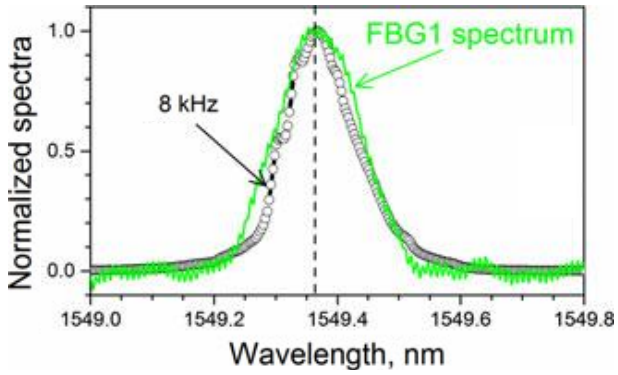

Figure 7. Typical optical spectrum in an F-P configuration. Normalized optical spectrum measured at a repetition frequency of 8 kHz (with circles) and a normalized reflection spectrum of FBG1 (continuous line). Adapted from [11].

Another effect arising when the peak power of AQS pulses exceeds 200 W, is that in the optical spectrum of AQS-pulses, two sidebands around the laser emission line appear (seen in Figure 8). This effect was recently attributed by Kolpakov *et al*. [18] to the amplified spontaneous emission observed at low repetition frequencies because the active fibers acquire considerable charge during the relatively long time interval between adjacent AQS pulses. However, 2009 Dudley *et al*. [31] demonstrated that these sidebands are the characteristic spectral sidebands which arise around the laser wavelength and are given by modulation instability (MI), the feature that will be discussed in Chapter 5.

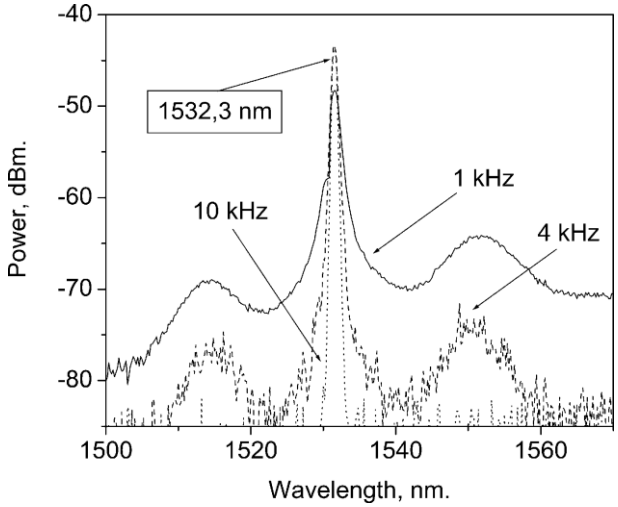

Figure 8. Spectra of AQS pulses recorded for 1 kHz (solid line), 4 kHz (dashed line) and 10 kHz (dotted line). The laser central wavelength is 1532.5 nm, and the sidebands are separated by approximately 11 nm from it. Adapted from [18].

The above examples highlight the main issues of AQS in F-P EDFL in temporal and spectral domains that exist in the literature till now; in the following section, we will analyze the temporal and spectral characteristics of AQS EDFL within the ring cavity.

2.2.2 AQS EDFL with ring cavity

All the fiber components described so far was used to make the AQS EDFL with the common F-P resonator. Another laser configuration that has been used for study is based on the ring resonator shown schematically in Figure 9. This configuration is, at least in theory, simple in the implementation of a ring resonator with two counter-propagating pump waves. The main feature of this arrangement is its simplicity, when one needs to use at least one WDM to inject the pump wave to an active fiber in one direction only, the optical isolator to maintain one directional laser operation, AOM to manipulate the Q-factor of the cavity, the active medium (rare-earth doped fiber) [10], and the filter to select a lasing wavelength. In our case, AQS fiber laser without any optically selective components (thus, with very broad laser line) was chosen for comparing its features with those of the narrow-band AQS laser with F-P cavity. Also, to simplify the laser arrangement, only one WDM is used for pumping the active fiber.

There are two possible realizations of the ring laser cavity, which depend on the direction of light-wave propagation determined by the isolator, namely the clockwise (CLW) and the counter-clockwise (CCW) ones, the latter is shown in Figure 9. The light wave is a major difference between the linear (F-P) and ring cavities. Another significant difference lies in the feedback mechanism of the cavity, namely in the way in which the laser wave is returned to the gain medium back. In the case of a linear cavity, as shown in Figure 3, the laser wave is reflected, it back to the same end of the gain fiber from both sides of the cavity, and only portion of the laser wave transmitted through the output coupler is used as the laser output. In contrast, in a ring cavity with a fiber coupler used as the laser output, the laser wave leaving from one end of the gain fiber will be injected into its opposite end. With such difference, the AQS dynamics in the laser with the ring cavity is expected to be different from that observed in the laser with F-P cavity. It is worth to notice that the round-trip time for a ring cavity is approximately half of the one measured in a linear cavity when the cavities are with the same lengths.

Similar to the energy evolution in the linear cavities, in each ring schemes (CLW and CCW) the laser wave starts to circulate after AOM opening (with a simultaneous frequency shift of 110 MHz at each round-trip, not of 220 MHz as in the case of the laser with F-P cavity). In both schemes, the final output pulse energy depends on repetition rate because the active fiber charge found just before

AOM switching ON depends on charging time (the interval between two neighbors AOM open states). It is seen that the output pulse energy in CCW scheme is much higher than that in the CLW scheme.

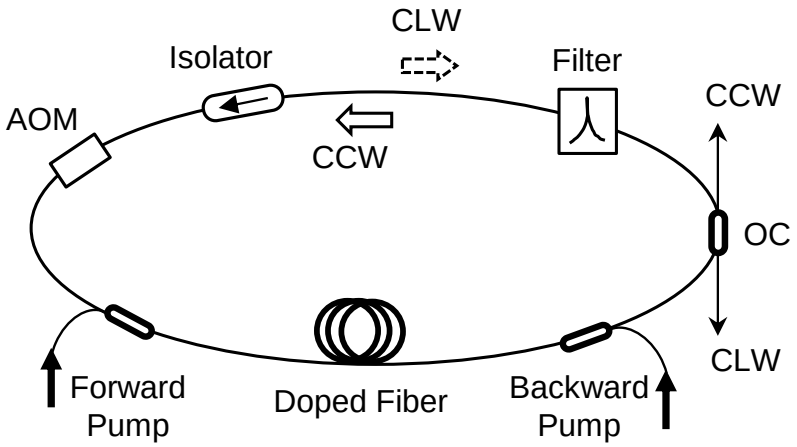

Figure 9. Scheme of a Q-switched fiber laser in a ring configuration.

The higher energy value is because the output pulse in the CLW case suffers from more losses given by the isolator return loss (~30 to 50 dB). Compared with the linear cavity previously discussed, the efficiency in the ring cavity is higher, this is attributed to a reduced cavity loss in the latter. In fact, in a roundtrip, the light-wave passes through the AOM (relatively high-loss, ~3 dB for one pass) in the ring cavity but twice in the linear cavity. The influence of the cavity loss on laser efficiency is more significant at higher repetition rate due to more round trips of the laser wave until the active fiber discharges.

Similarly to the discussion on the linear cavity, one can analyze the Q-switching characteristics of the laser with the ring cavity under different domains. Though the dynamics may be different, the physical mechanism of the pulses splitting is similar. In the following discussions, we will present some typical results for the laser assembled in the ring configuration.

Temporal Domain

A laser with a backward-pumped ring cavity and without optical filter is shown in Figure 10 (a). In this type of cavity, the multi-peak structure of the output pulse is formed as follows. The seed of a laser pulse is ASE from the EDF, which waits for AOM switching ON at its entrance. After AOM switching ON, ASE wave starts to propagate along the cavity. When the AOM rise time is short compared with the round-trip time, the leading edge of the ASE wave repeats AOM switching ON function (see

Figure 5 (a)). After AOM opening, the ASE wave travels around the ring cavity with periodic amplification in the EDF until the population inversion is substantially depleted. Since an output pulse from the laser is a sequence of the partially extracted ASE wave traveling around the amplifying ring cavity for several times, its shape presents a multi-peak structure with sub-pulse number corresponding to a number of its passes along the cavity. Furthermore, the sub-pulses become "triangular" due to partial EDF discharging (population inversion decreasing) by each consequent sub-pulse. An experimental trace of typical AQS pulse from the laser with ring cavity is shown in Figure 10 (b); in this laser, the cavity length was 25 m (this gives a round-trip time near to 120 ns) and the AOM rise time was 100 ns.

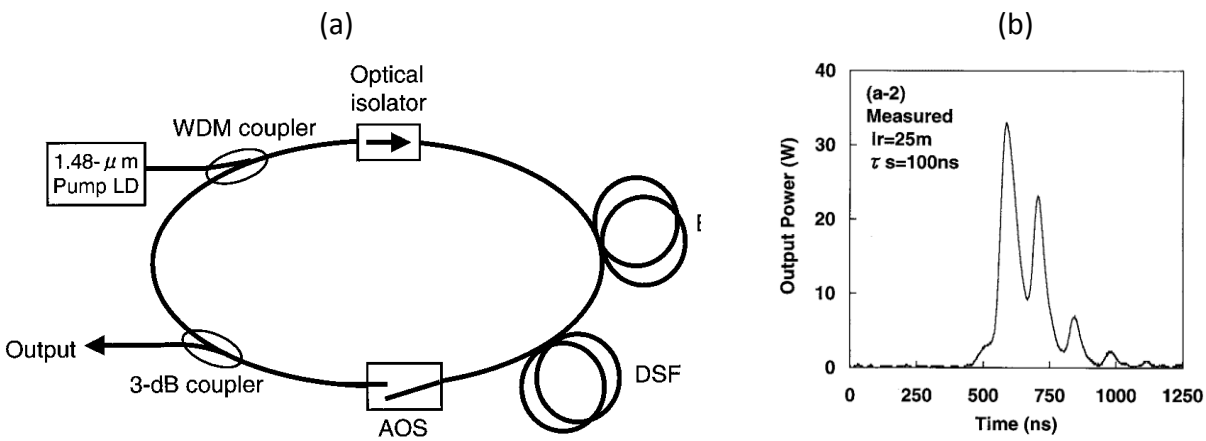

Figure 10. (a) Diagram of forward pumping ring cavity. (b) AQS pulse from a fiber laser with ring cavity without an optical filter. The cavity length was 25 m (the round-trip time is near to 120 ns) and the AOM rise time was 100 ns. AOS and DSF stand for acousto-optic switch and dispersion-shifted fiber, respectively. Adapted from [32].

Spectral Characteristics

In the following chapter, a systematic experimental and theoretical investigation of the spectral dynamics of giant pulses from AQS EDFL based on the ring cavity without spectral filtering is provided.

2.2.3 Modeling a Q-Switched Erbium-Doped Fiber Laser

Previously, optical and electronic properties of the Er^{3+} ions in a silica matrix have been discussed. These properties are the basis to derive a set of the balance equations in the case of a simplified five-level energy scheme of Er^{3+} when pumped at 980 nm (see Figure 11 (a)) or at 1480 nm (see Figure 11 (b)), which can be further described as a typical initial-boundary-value problem. The guidelines for the derivation of this system of partial differential equations (PDE) are described in details by Kolpakov *et al*. in [8] and the references therein.

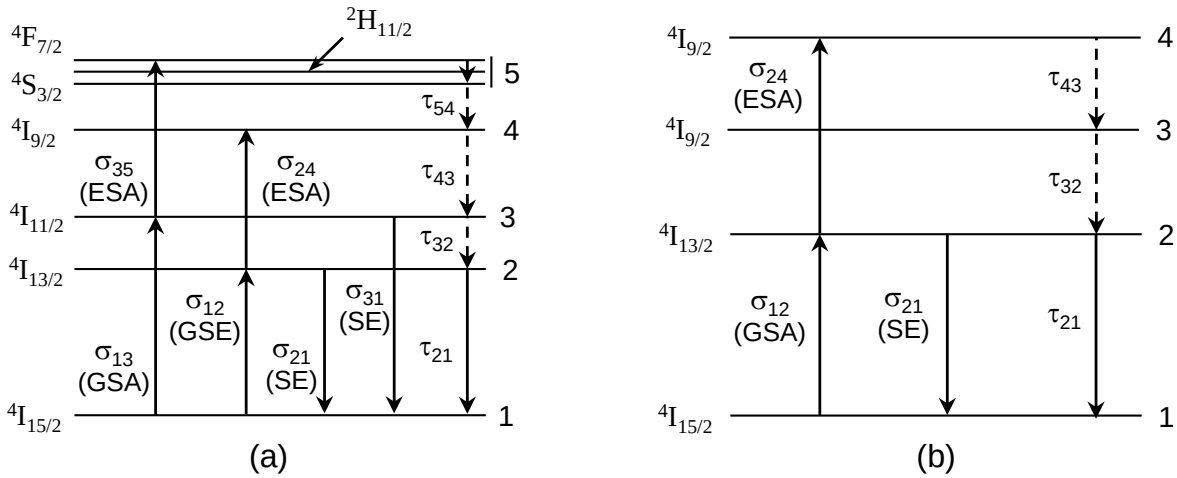

Figure 11. (a) Simplified five-level energy scheme of Er^{3+}, pumping at 980 nm, adapted from [8]. (b) Simplified four-level energy scheme of Er^{3+}, pumping at 1480 nm. The radiative (photon-induced) transitions are shown by the solid arrows and the non-radiative (phonon-assisted) relaxations by the dashed arrows, σ_{ij} and τ_{ij} represent, respectively, the cross-sections and the decay times for the transitions between the levels i and j.

The five-level energy scheme is used when EDF is pumped at 980 nm. It takes into account all radiative and non-radiative transitions and the set of balance equations describing the whole processes involved at pumping EDF are as follows:

$$\frac{\partial N_2}{\partial t} = \frac{\sigma_{12}^{s} I_s}{h\nu_s} N_1 + \frac{\sigma_{12}^{se} I_{se}}{h\nu_{se}} N_1 - \frac{\sigma_{21}^{s} I_s}{h\nu_s} N_2 - \frac{\sigma_{21}^{se} I_{se}}{h\nu_{se}} N_2 - \frac{\sigma_{24}^{s} I_s}{h\nu_s} N_2 - \frac{\sigma_{24}^{se} I_{se}}{h\nu_{se}} N_2 - \frac{N_2}{\tau_{21}} + \frac{N_3}{\tau_{32}}, \tag{1.1}$$

$$\frac{\partial N_3}{\partial t} = \frac{\sigma_{13} I_p}{h\nu_p} N_1 - \frac{\sigma_{31} I_p}{h\nu_p} N_3 - \frac{N_3}{\tau_{32}} - \frac{\sigma_{35} I_p}{h\nu_p} N_3 + \frac{N_4}{\tau_{43}}, \tag{1.2}$$

$$\frac{\partial N_4}{\partial t} = \frac{\sigma_{24}^{s} I_s}{h\nu_s} N_2 + \frac{\sigma_{24}^{se} I_{se}}{h\nu_{se}} N_2 - \frac{N_4}{\tau_{43}} + \frac{N_5}{\tau_{54}}, \tag{1.3}$$

$$\frac{\partial N_5}{\partial t} = \frac{\sigma_{35} I_p}{h\nu_p} N_3 - \frac{N_5}{\tau_{54}}, \tag{1.4}$$

$$N_0 = N_1 + N_2 + N_3 + N_4 + N_5. \tag{1.5}$$

Here and in the sets of equations below $N_k = N_k(z,t)$ are the Er^{3+} levels' populations ($k = 1,\ldots,5$) that depend on position and time along the active fiber, h is the Plank constant, ν_p, ν_s and ν_{se} are the optical frequencies of the pump, signal (laser) and ASE waves, σ_{ij} are the cross-sections for the transitions $i \to j$ (superscripts and subscripts *s*, *se*, and *p* indicate that the parameter refers to the

signal, the spontaneous emission, signal (laser) and pump wavelengths), τ_{ij} are the decay times between the levels i and j, I_p, I_s and I_{se} are the intensities of the pump, the signal and ASE waves, N_0 is the Er^{3+} ions' concentration in the EDF core. It is considered that the Er^{3+} ions are distributed over the fiber core homogeneously and their concentration outside the core is zero. The intensities in the equations shown above are taken on the fiber axis and their values are obtained from the corresponding pump, laser, and ASE powers normalized to the Gaussian beams' areas.

Figure 11 (b) presents a four-energy scheme used when EDF is pumped at 1480 nm. The set of balance equations describing the whole processes involved at 1480 nm pumping EDF are as follows:

$$\frac{\partial N_2}{\partial t} = \frac{\sigma_{12}^p I_p}{h\nu_p} N_1 + \frac{\sigma_{12}^s I_s}{h\nu_s} N_1 + \frac{\sigma_{12}^{se} I_{se}}{h\nu_{se}} N_1 - \frac{\sigma_{21}^p I_p}{h\nu_p} N_1 - \frac{\sigma_{21}^s I_s}{h\nu_s} N_2 - \frac{\sigma_{21}^{se} I_{se}}{h\nu_{se}} N_2 - \frac{\sigma_{24}^p I_p}{h\nu_p} N_2 - \frac{N_2}{\tau_{21}}, \tag{2.1}$$

$$\frac{\partial N_3}{\partial t} = \frac{N_4}{\tau_{43}} - \frac{N_3}{\tau_{32}}, \tag{2.2}$$

$$\frac{\partial N_4}{\partial t} = \frac{\sigma_{24}^p I_p}{h\nu_p} N_2 - \frac{N_4}{\tau_{43}}, \tag{2.3}$$

$$N_0 = N_1 + N_2 + N_3 + N_4. \tag{2.4}$$

The proper set of differential equations describing the spatial-temporal evolution of the pump, two counter-propagating signal waves, and the ASE, are derived using the fundamental law of conservation of energy through the energy flux. These equations are written as:

$$\left(\frac{n_p}{c}\frac{\partial}{\partial t} - \frac{\partial}{\partial z}\right) P_p(z,t) = -\alpha_p(z,t) P_p(z,t), \tag{3.1}$$

$$\left(\frac{n_s}{c}\frac{\partial}{\partial t} \pm \frac{\partial}{\partial z}\right) P_s^{\pm}(z,t) = g_s(z,t) P_s^{\pm}(z,t) + \frac{\delta\Omega}{4\pi}\eta \frac{N_2(z,t)}{\tau_{21}} h\nu_s \pi a^2, \tag{3.2}$$

$$\left(\frac{n_{se}}{c}\frac{\partial}{\partial t} \pm \frac{\partial}{\partial z}\right) P_{se}^{\pm}(z,t) = g_{se}(z,t) P_{se}^{\pm}(z,t) + \frac{\delta\Omega}{4\pi}(1-\eta) \frac{N_2(z,t)}{\tau_{21}} h\nu_{se} \pi a^2, \tag{3.3}$$

where n_p, n_s, and n_{se} are the modal indices for LP_{01} propagation mode at the pump, laser, and SE wavelengths, c is the free-space light velocity, P_p is the pump power (the pump wave propagates to

the left direction), $P_s^{\pm}$ are the powers of the signal (laser) waves, $P_{se}^{\pm}$ are the ASE powers (the convention adopted is that the wave propagating in the right direction is labeled by a superscript "$+$" and the one traveling to the left direction by a superscript "$-$"), α_p is the fiber core absorption at the pump wavelength ($\lambda_p = 975$ nm or 1480 nm), and a is the EDF core radius. The gain g_s is calculated at the laser wavelength ($\lambda_s = 1550$ nm) and the gain g_{se} at the SE wavelength (λ_{se}=1530 nm). The geometric factor $\delta\Omega / 4\pi$ is the fraction of the ASE photons captured by the fiber core. The variable $\eta = g(\lambda_s)\Delta\lambda_s / \Delta\lambda_{Er}$ is the spectral fraction of ASE power reflected by spectrally selective mirrors, $g(\lambda_s)$ is the normalized lineshape function at the laser wavelength, $\Delta\lambda_s$ is the laser line-width, and $\Delta\lambda_{Er}$ is the effective Er^{3+} emission line width. The second term on the right side of eq. (3.2) is the small fraction of the whole fluorescence power added to the signal power of the short fiber segment dz, while in eq. (3.3), it is the fluorescence power added to the ESA power for the same fiber segment.

The pump absorption and signal gain are written as

$$\alpha_p(z,t) = \alpha_{p0}\left[n_1(z,t) - (\xi_p - \varepsilon_p)n_3(z,t)\right] + \alpha_{BG}, \tag{4.1}$$

$$g_s(z,t) = \alpha_{s0}\left[(\xi_s - \varepsilon_s)n_2(z,t) - n_1(z,t)\right] - \alpha_{BG}, \tag{4.2}$$

$$g_{se}(z,t) = \alpha_{se0}\left[(\xi_{se} - \varepsilon_{se})n_2(z,t) - n_1(z,t)\right] - \alpha_{BG}, \tag{4.3}$$

where α_{s0}, α_{p0}, and α_{se0} are the small-signal absorption coefficients for the laser, pump and SE wavelengths, α_{BG} is the fiber background loss measured in the range from 1100 to 1200 nm (the erbium transparency window), $\xi_{s,se} = \sigma_{21}^{s,se} / \sigma_{12}^{s,se}$, $\xi_p = \sigma_{31} / \sigma_{13}$, $\varepsilon_p = \sigma_{35} / \sigma_{13}$, $\varepsilon_{s,se} = \sigma_{24}^{s,se} / \sigma_{12}^{s,se}$ are the ESA parameters at the pump, signal, and SE wavelengths.

Finally, the laser initial-boundary conditions associated with the above partial differential equations depend on the cavity structure and Q-switching process. For a forward pumping F-P scheme are written as follows:

$$P_p(z=0,t) = P_{p0}, \tag{5.1}$$

$$P_s^{+}(z=0,t) = P_s^{-}(z=0,t)R_1 t_1^2, \tag{5.2}$$

$$P_s^-\left(z=L_c,t\right)=P_s^+\left(z=L_c,t\right)R_2t_2^2\left(F_{AOM}\left(t\right)\right)^2, \tag{5.3}$$

$$P_{se}^+\left(z=0,t\right)=P_{se}^-\left(z=L_c,t\right)=0, \tag{5.4}$$

where P_{p0} is the pump power at the EDF entrance, $R_{1,2}$ are the FBGs reflection coefficients, L is the EDF length, L_c is the cavity length measured from the left FBG (output coupler), and t_1 and t_2 are the transmission coefficients of the splices between EDF and other intra-cavity elements on the left side from AOM (t_1) and on its right side (t_2). The output powers at the laser output is given by

$$P_{\text{out}}\left(t\right)=\left(1-R_1\right)t_1P_s^-\left(0,t\right). \tag{6}$$

For a ring cavity the signs "+" and "-" stand for the clockwise and counter-clockwise direction (CCW), respectively. The boundary conditions for a backward pumping ring scheme and CCW signal detected are written as follows:

$$P_p\left(z=0,t\right)=P_{p0}, \tag{7.1}$$

$$P_s^-\left(z=L_c,t\right)=P_s^-\left(z=0,t\right)t_{oc}t_Ft_1F_{AOM}\left(t\right) \tag{7.2}$$

$$P_s^+\left(z=L_c,t\right)=0, \tag{7.3}$$

$$P_{se}^-\left(z=0,t\right)=P_{se}^+\left(z=L_c,t\right)=0 \tag{7.4}$$

where t_{oc} is related to the output coupler transmission, t_F is related to transmittance of the filter and the t_1 is the fiber splices losses. The cavity length is measured from the output coupler to the clockwise direction, and the output powers at the output port is given by

$$P_{\text{out}}\left(t\right)=\left(1-t_{oc}\right)t_1P_s^-\left(z=0,\text{t}\right) \tag{8}$$

To solve these equations, one should use the distributed model (also named as "traveling-wave method" [33]) that accounts for the spatial-temporal Er^{3+} populations' distributions. For these fiber lasers, the chromatic dispersion effect can be neglected due to a short fiber length; thus, n_k are considered as wavelength-independent, which equal to the modal index n_s. For the passive (no gain) fiber used in the cavity, such as fiber tails of AOM, WDMs and FBGs, one can set to zero populations of all levels of active ions. Finally, the AOM transmission function $F_{AOM}\left(t\right)$ is characterized by the following function [8], [13]:

$$F_{AOM}(t) = a\left[1-\cos\left(\pi\frac{t}{T_r}\right)\right]^b, \tag{9}$$

this function applies to the interval $0 < t < T_r$. In this equation T_r is the AOM rise-time and a and b are fitting parameters. For $t > T_r$ the value of the AOM transmittance reaches the maximum and then does not change.

It is worth to mention that nonlinear optical effects were not considered in the discussed model.

The comparison between the computer simulations and the experimental results are presented for an F-P cavity pumped from the right cavity side through 980/1550 WDM. The cavity length was $L_c = 10.3$ m that included a 4 m EDF from *Thorlabs*, model M5-980-125, AOM with output fibers, and two gratings FBG1 and FBG2 used as selective couplers with reflectivities of 89.4% (rear grating) and 37.6% (output grating), respectively [8]. Some examples of simulated and the experimental pulses for the F-P laser are shown in Figure 12, separately for each laser output.

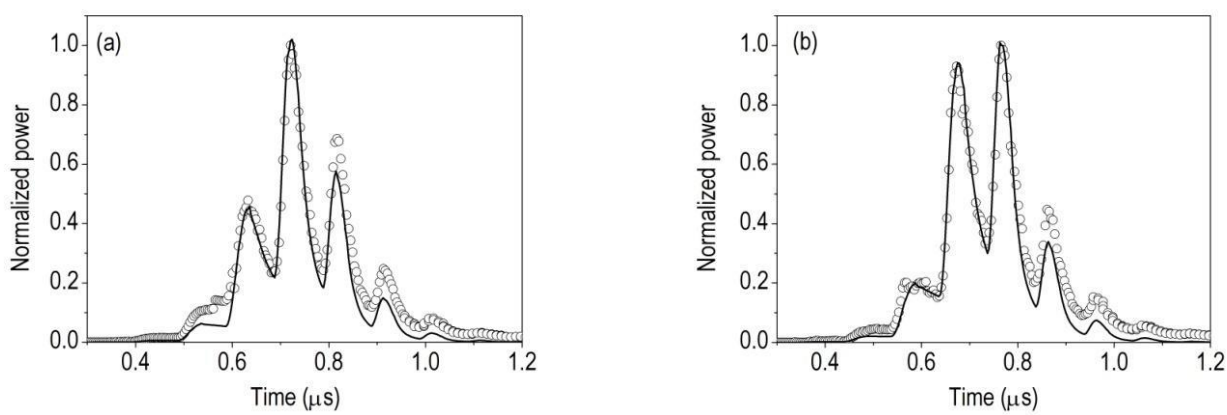

Figure 12. Theoretical (solid lines) and experimental (open circles) pulses registered from the opposite QS-EDFL, (a) the left and (b) the right. Adapted from [8].

It is worth mentioning that the origin of small differences between the experimental and the simulated data resides on the following factors: (*i*) the model does not take into account the radial distribution of the fundamental mode (for all wavelengths), (*ii*) the radial distribution of population of the Er^{3+} ion levels is ignored; this may lead to over- or under-estimation of the EDF absorption/gains coefficients and to some errors in estimation of the intra-cavity laser power and, consequently, to errors in the laser level's decaying dynamics, (*iii*) the narrowing of the laser optical spectrum that

takes place at each reflection by the selective cavity coupler, (*iv*) the comparatively slow drift of charge carriers in the photodiode [34], which has an effect on measuring the trailing edge of the pulse and (*v*) some more complex effects that are possibly ignored in the model.

2.3 Photon Statistics of AQS pulses

In this section, we will describe in details the photon statistics of AQS pulses, separately for each sub-pulse. In this study, we assume that the photodetector is an ideal device with photo-current statistics that replicate those of an incoming light signal. In fact, there no exist ideal photodetectors. Due to two principal reasons: first, even in absence of an input optical signal detectors demonstrate some background (dark) temperature-dependent output current with thermal noise characterized by Gaussian distribution and, second, due to undesirable recombination of photo-induced electron-hole pairs the conversion efficiency of incident photons to pairs of carriers is always less than 100%.

Factors as electronic noise, non-linearity of photodiodes and of following pre-amplifiers all influence the photon statistics as well. These undesirable properties of real photo-receivers are out of the scope of this thesis. However, to diminish the influence of the negative effects noted above, in our experimental circumstances we maintained the equivalent power (NEP) of photoreceiver's background noise accounted for the whole detector RF band to be much less than laser power measured on the photoreceiver's entrance.

All of the following sources, fluorescent and incandescent light bulbs, the Sun, and the amplified spontaneous emission of optical amplifiers are examples of incoherent light (also known as thermal light or chaotic light or incoherent light). The photon statistics of these sources are well described by Bose-Einstein (BE) statistics [35], [36]. On the other hand, the photon noise statistics of the coherent light sources as, for instance, monochromatic light from continuous wave lasers, is described by Poisson distribution [35], [36]. However, as discussed below, when the photodetector RF band is limited from above so that the optical band is much broader (by orders) than the RF band measured in Hertz, the photon statistics is also described by Poisson distribution. In the intermediate case, when the photodetector RF band is comparable to the bandwidth of the light source, the latter plays a significant role in a type of the photon statistics that is different from the Poissonian one.

In particular, we further reveal that light sources as actively Q-switched fiber lasers, exhibit B-E or Poissonian photon statistics, depending on a ratio of the optical band of light to the RF band of the photodetector. This ratio will be used below for definition of a number of orthogonal modes M filling the light spectrum: $M = sBT$, where *s* is a number of polarization states ($s = 2$ in the case of non-polarized light), B is the ASE optical bandwidth (in Hertz), and T is the reciprocal RF bandwidth of the photodetector used (or counting time). These modes are orthogonal since the photon noise presented in each mode does not correlate with that of any other modes. Note also that when the optical band of ASE equals to the RF band of the photodetector and the light is polarized, only one mode exists ($M = 1$). Warning: the term *modes* used here is not associated with the laser cavity modes which are not established in our case because of optical frequency shift in the AOM and only a few round trips realized by filtered ASE along the laser cavity until the AQS pulse is developed, and with the spatial modes existing in multimode fibers. Note also that the case of multimode fibers is out of the scope of the presented work.

If ASE of optical amplifier is optically filtered (by narrow-band FBGs in our case) so that the optical bandwidth B is comparable to the photodetector RF band $1/T$, the photon statistics obeys the $M_{\mathrm{BE}}-$fold degenerate Bose-Einstein distribution (the sub-script *BE* stands for B-E distribution; see refs. [37]–[40], [41, Ch. 13] and references therein), as stems from the photon counting statistics, namely the birth-death immigration statistics in a traveling-wave amplifier [38], [41, Ch. 13]:

$$P\left(n,\bar{n},M_{BE}\right)=\frac{\Gamma\left(n+M_{BE}\right)}{\Gamma\left(n+1\right)\Gamma\left(M_{BE}\right)}\frac{\left(\bar{n}\right)^{n}}{\left(1+\bar{n}\right)^{n+M_{BE}}}, \tag{10}$$

where $M_{\mathrm{BE}} = sBT$, $\bar{n} = \bar{n}_{BE} / M_{BE}$ is the mean photon number of filtered ASE per mode, $\bar{n}_{BE} = WT / h\nu$ is the mean photon number of non-filtered ASE, W is the optical power, h is the Plank constant, and ν is the central spectrum frequency of the filtered light.

The photon distribution described by eq. (10) corresponds to the negative binomial distribution [41, Ch. 13]. For the single mode amplifier ($M_{BE} = 1$), this distribution reduces to the well-known *Bose-Einstein* (no degenerate) distribution:

$$P\left(n,\bar{n}\right)=\frac{1}{1+\bar{n}}\left(\frac{\bar{n}}{1+\bar{n}}\right)^{n}. \tag{11}$$

On the other hand, when $M_{BE} = M_P \to \infty$ that is the case of non-filtered ASE, distribution described by eq. (10) tends to the Poisson distribution [41]:

$$P(n, \bar{n}, M_P) = \frac{\bar{n}^n e^{-\bar{n}}}{n!}, \tag{12}$$

where $\bar{n} = \bar{n}_P / M_P$, and $\bar{n}_P = WT / h\nu$ is the mean photon number of non-filtered ASE found in all existing M_P modes filling the whole ASE spectrum.

Examples of the photon statistics for non-polarized light ($s = 2$) are given in Figure 13 for Poissonian and Bose-Einstein distributions, which are normalized to their maxima and according to their most probably photon values. It is seen that the broadest and strongly asymmetrical BE distribution is observed at $M_{BE} = 2$, i.e., when two polarization modes exist and $B_{\mathrm{BE}}T = 1$ (so the optical bandwidth equals to the RF band of the photodetector), whereas at increasing M_{BE} it becomes narrower and more symmetrical, approaching Poissonian one at $M_{BE} \to \infty$.

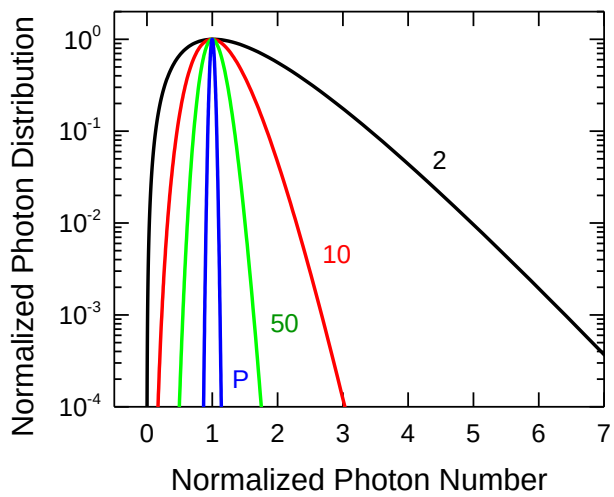

Figure 13. Normalized photon distributions versus photon number normalized to their most probable values, simulated for 10^3 photons. The curve marked as P corresponds to the Poissonian statistics, whereas other curves are marked with M_{BE} used at simulating Bose-Einstein photon distributions.

An important feature observed in photon statistics is that the width of the normalized Poissonian distribution depends on the photon number acquired, whereas it "saturates" as increases the photon number ($>10^2$) in the normalized Bose-Einstein distribution. As an example, several histograms simulated for these two types of distributions, obtained at different mean photon numbers, are shown in Figure 14.

As seen from Figure 14, a histogram's character is defined, when increasing photon number, by the type of photon statistics. That is, in Poissonian statistics, the bigger the photon number, the narrower the distribution; in the meantime, in the case of Bose-Einstein statistics, the normalized histograms do not change with the mean photon number exceeding $\sim 10^2$. The found laws are important for the discussion presented below.

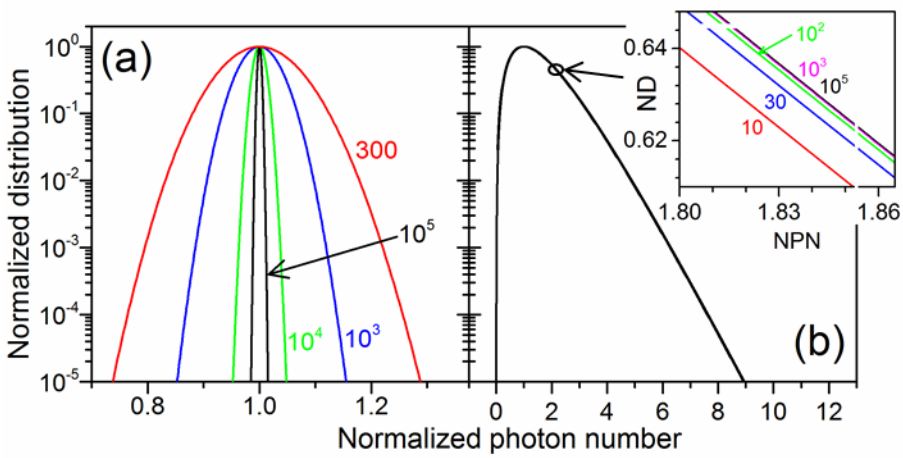

Figure 14. Normalized photon distributions versus photon number normalized to their most probable values, simulated for (a) Poissonian and (b) Bose-Einstein ($M_{BE} = 2$) statistics for different photon numbers (marked near each curve). Inset to (b) shows the small section of the Bose-Einstein distributions (presented in the mainframe and marked by the ellipse) in the linear scale with a high scaling factor; ND is normalized distribution, and NPN is normalized photon number.

Chapter 3 Spectral Dynamics

This chapter describes the results of the experimental study carried out for Q-switched fiber lasers assembled in two geometries, F-P and ring, with focus on the temporal and spectral dynamics. The physics behind the laser dynamics is discussed in detail for both laser configurations.

3.1 Experiment setup

The two laser configurations used in this experiment are shown in Figure 15, the upper sketch (a) corresponds to the laser assembled in the F-P geometry, and the lower one (b) in the ring geometry. In both cases, commercial EDF (*Liekki*, ER16-8/125) was used as a gain medium, with length of 4 m in F-P and 6 m in ring configurations. It is important to mention that at bigger EDF lengths FLs generate CW emission despite the AOM is switched *off*; this regime is not desired hence is suppressed. The fiber coupled AOM (*A-A Opto-Electronic*, MT110-IIR25-3Fio-SM5-J1-A) was used for Q-factor modulating. The data sheet from the manufacturer states that the maximum of diffraction efficiency to the first order for 1550 nm (the laser wavelength) is $\sim 40\%$. The AOM1 operates at a fixed RF of 110 MHz with a rise-time of 50 ns that is less than the Q-switched pulse buildup.

The F-P cavity is formed by two home-made FBGs written in a photosensitive fiber (*Fibercore* PS1250/1500) that have waveguide parameters similar to the EDF used in the lasers setups, with reflectivity 24% (FBG1, is used as the output coupler) and 99.8% (FBG2, the rear coupler). Both FBGs were centered at 1548.1 nm (laser wavelength, see Figure 16 (a) for FBGs spectra). Meanwhile, a 20:80% multiplexer for 1550 nm (*Opto-Link Corporation Ltd.*) with SMF-28 fiber tails was used as the output coupler in ring geometry. Note that the output coupling in these two cases was of approximately the same value.

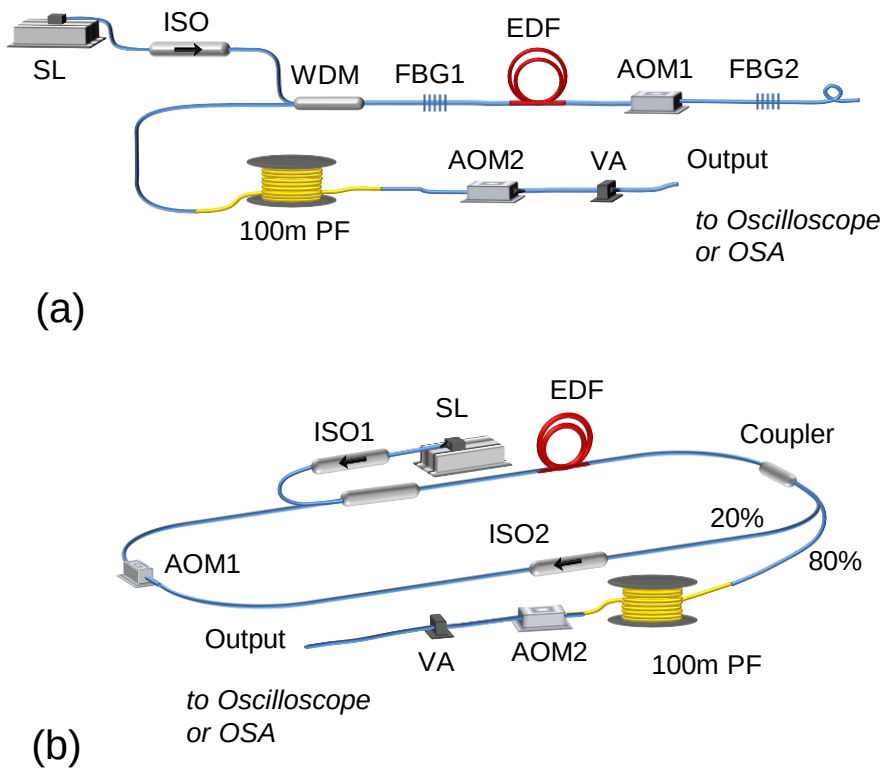

Figure 15. Schematic diagrams for AQS EDFLs assembled in (a) F-P and (b) ring geometries.

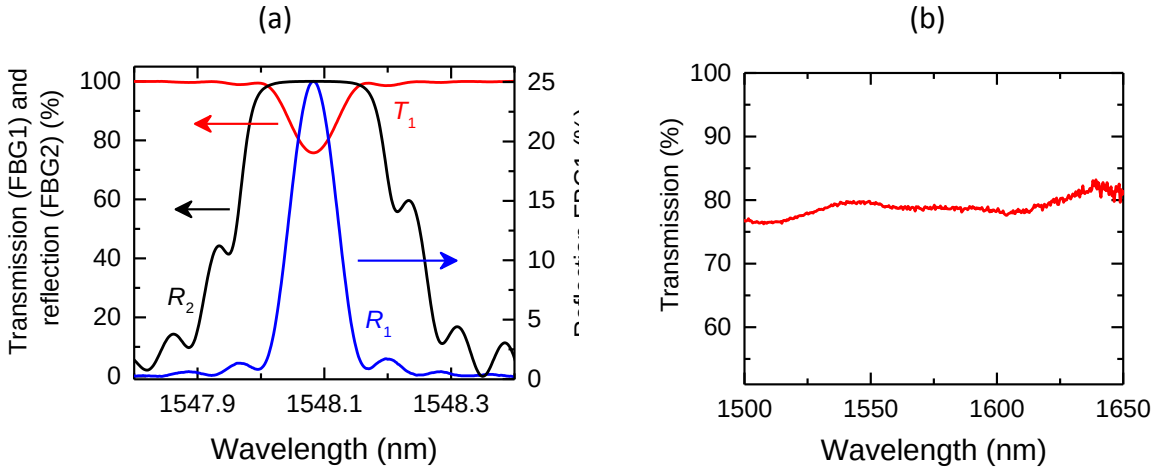

Figure 16. (a) Transmission and reflection spectra of FBGs centered at 1548.14 and captured by OSA with 20-pm resolution. (b) 20:80% multiplexer transmission spectrum obtained experimentally in a broad optical band.

For both lasers: the pump laser is a standard fiber-coupled semiconductor laser (SL) operated at 1480 nm with power fixed at its maximum, 400 mW (*JDSU*). The SL fiber tail was spliced with a fibered isolator (ISO) at 1550 nm, which protected SL against damaging by AQS pulsing. The output 2 of the first WDM in F-P scheme was considered as low-power laser output. In the ring cavity, only one WDM

is used, and it serves as pump coupling. In both lasers, the maximal SL power transmitted by the set of ISO and WDM/WDMs to the laser entrances were 260 mW and 268 mW in the F-P and the ring set-ups, respectively. The main sources of such high optical losses were the ISO loss (up to 1.3 dB at 1480 nm) and the losses of WDMs and fiber splices.

First, the central wavelength of the FBG1 was tuned by applying mechanical stretch. The spectrum was measured at the output by using an optical spectrum analyzer (OSA) (*Yokogawa* AQ6370B) with a resolution of 20 pm, see Figure 17, before and after tuning the FBGs. The FBG1 central wavelength shifts to longer wavelengths as the strain is increased. So, to find the correct tuning, the intra-cavity ASE generated in EDF was used as a light source. The AOM1 was always kept in the ON state, and the pump rate was chosen to be below the CW laser threshold. The FBG1 transmission spectrum and the FBG2 reflection spectrum were obtained due to ASE transmission through FBG1 and its reflection from FBG2 (see Figure 16 (a)). Once the optimum spectral overlapping was obtained, the F-P cavity was ready to be used in experiments. For the ring cavity, there was no need of any tunings due to the absence of FBGs.

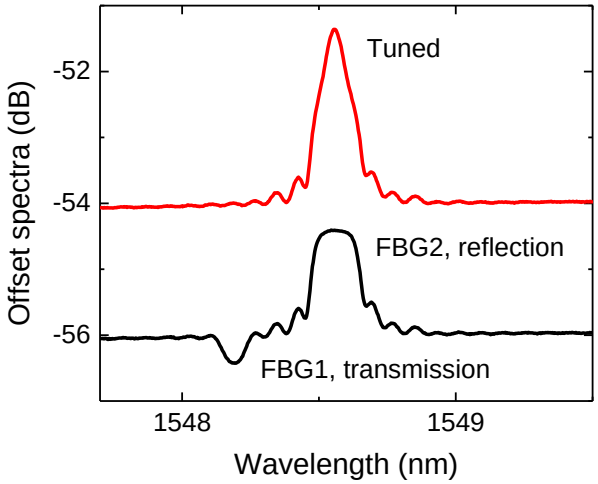

Figure 17. Spectra measured on the F-P laser output below EDFL threshold when FBGs are free (not tuned) (black line) and when they are mechanically tuned FBGs (red line).

3.2 Temporal and energy characteristics of AQS pulses

The AQS-FLs were characterized by studying various parameters under different operating conditions, but always keeping constant the pump power at values noted above. Both the lasers were tested at the same AOM1 repetition rates, which varied from 50 Hz to 50 kHz. The AOM1 ON time

(AOM1 gate) was adjusted to obtain stable Q-switched pulses in both amplitude and time. Figure 18 demonstrates the pulses' waveforms as a function of the AOM1 repetition frequency: Figure 18 (a) shows the pulse waveforms for F-P geometry, and Figure 18 (b) shows the pulse waveforms for the ring geometry. Pulses were delayed concerning the moment when the AOM was switched ON (this moment $t = 0$, will be considered below as zero-time). The digitized waveforms presented in Figure 18 were averaged over 100 measurements. The pulses, in this case, were detected by a photoreceiver 1611 (*New* Focus, 1 GHz RF bandwidth) then were digitized by an oscilloscope DPO7354C (*Tektronix*, 3.5 GHz RF bandwidth), which was triggered by the function generator synchronously with the AOM1 driver. Finally, the vertical scale units were rescaled from Volts to Watts using the following procedure: first, the energy per pulse was computed by

$$E = \frac{\bar{P}}{f_{rep}}, \tag{13}$$

where $\bar{P}$ is the average (CW) output power and f_{rep} is the AOM1 repetition rate, then each data point was multiplied by the energy and divided by the total numerical integration of the pulse. The energy ratio from eq. (13) was taken after subtracting the ASE background power, as high as 0.3 mW for F-P and 1.5 mW for ring lasers.

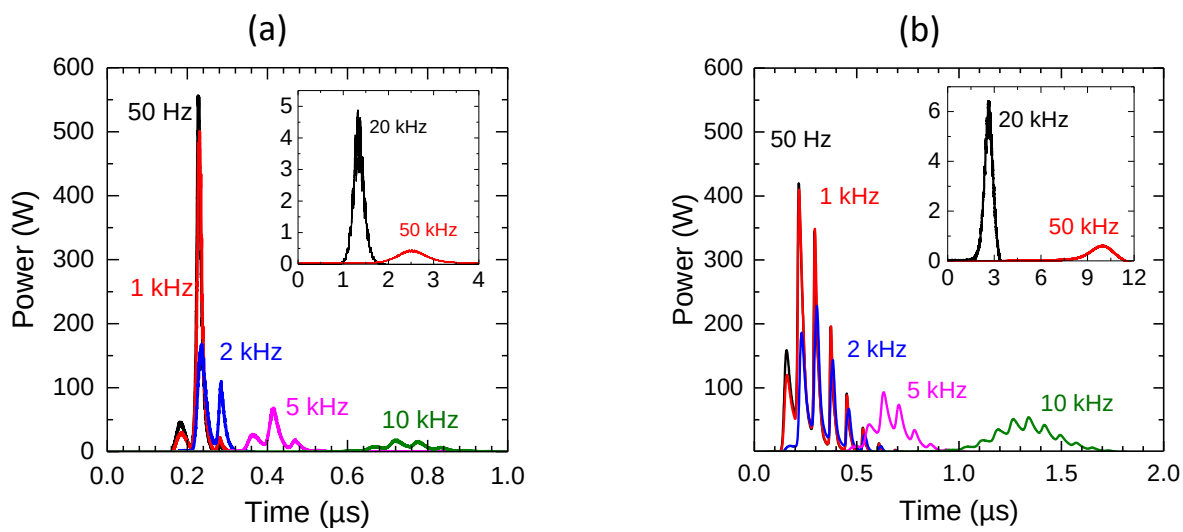

Figure 18. Waveforms of AQS pulses measured from (a) F-P and (b) ring lasers *vs*. AOM1 repetition rate. Zero-time corresponds to the moment of AOM1 switching ON.

The AQS-FLs were first characterized regarding the energy per pulse and peak power, both versus AOM1 repetition frequency; the result of this study is shown in Figure 19. From this figure, one

can compare these parameters for AQS pulses obtained from the lasers with F-P (red filled circles) and ring (black filled squares) configurations shown for repetition rates varied in the range from 50 Hz to 50 kHz. For repetition frequencies higher than 50 kHz no stable pulse train was obtained since the pulse build-up time is longer than the interval when AOM1 is closed (in this case the lasers operates in a regime of chaotic pulses [42].

In our experiments, a repetition rate greater than 1 kHz causes a reduction in pulse energy and peak power due to the finite recovery time of the population inversion, which is directly related to pump power and the lifetime of the metastable level, typically 10 ms for the erbium ion. Below 1 kHz, the population inversion recovers during the interval when AOM1 closed until the same level defined by ASE. Only small variations in the pulse shape and energy are observed in this range of repetition rates. Also, Figure 19 (left side) shows that energy of AQS pulses extracted from the F-P laser is lower than that from the ring one. Such behavior results from higher round-trip loss for the laser with F-P cavity (around 9 dB per round-trip) occurring due to double passing of the laser wave through AOM and numerous fiber splices inside the cavity, whereas in the ring cavity these losses are counted only for one time (~ 4.5 dB). In contrast, AQS pulses from the F-P laser are more powerful than ones from the ring laser (see Figure 19, right side), the effect arising from the fact that a sub-pulse number in the first case is smaller than in the second case. The peak power was obtained from Figure 18.

The pulse waveforms and energies, as shown in Figure 18 and Figure 19, were almost of the same values for repetition frequencies ranging from 50 Hz to 1 kHz. However, for repetition rates lower than 1 kHz, the OSA measurements are not so precise due to fewer optical pulses per OSA integration time. In addition, if the optical attenuation is decreased for such lower frequencies, the OSA response may be saturated due to detecting AQS pulses with high peak power. On the other hand, for higher frequencies (above 1 kHz), some nonlinear optical effects due to lower peak power are reduced. Therefore, we suppose that 1 kHz is an optimum repetition frequency to study the pulse characteristics.

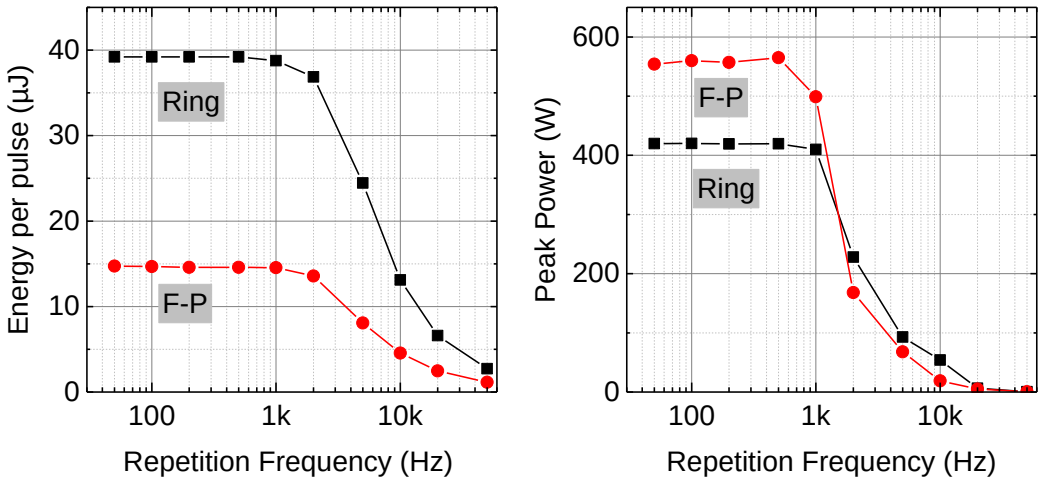

Figure 19. Energy per pulse is given by eq. (13) (left) and pulse peak power (right) *vs*. repetition rate. These values were estimated after accounting for CW (averaged) power from the lasers' outputs, ASE contribution from spectral measurements with OSA, and waveforms of AQS pulses.

In the next part of the experimental work, the AOM1 repetition frequency and its transparency gate time were set at 1 kHz and 2µs, accordingly. Then, in all sets of experiments, we maintained fixed pump rates at values mentioned above. The experiments consisted on two main parts: the first one was focused on the study of the sub-pulses' spectra for both F-P and ring cavities whereas the second one - on the study of the sub-pulses' spectral and noise properties after propagating along 100 m SMF-28 fiber. Later onwards, the temporal characteristics will be discussed in Chapter 4 for both cases.

As the first part of the experimental study, the temporal shapes of the laser pulses at a repetition rate of 1 kHz were collected; the result is presented in Figure 20. The traces of AQS pulses were averaged over 100 realizations. The AQS pulses are composed of several sub-pulses, separated by 60 ns (Figure 20 (a)) and 80 ns (Figure 20 (b)), corresponding to the cavity lengths of 6.2 m and 16.5 m for the lasers realized with F-P and ring cavities, respectively. The highest sub-pulses are the fourth (F-P) and the third (ring) ones, having the peak powers of 500 W and 410 W, and full width at half of its maximum (FWHM) of 19 ns and 27 ns, accordingly for F-P and ring lasers. Note that these sub-pulses, characterized by highest peak power and energy, will be designated as the "mains" in further discussion.

From Figure 19 we found the whole QS pulse energy of approximately 15 µJ (F-P) and 40 µJ (ring). Note that the number of distinguishable (in linear scale, see upper panels in Figure 20) sub-pulses in the F-P laser is less than that in the ring one, given that the ASE passes twice the EDF cavity

at each round-trip in the former case while only once in the latter case. As can be seen in both laser configurations, the sub-pulses are not symmetric in shape since the sup-pulses fronts are determined by the AOM1 rise time whereas the long decay time at the trailing edges by the depopulation in the laser level, $^4I_{13/2}$, of the erbium ions [8], [43].

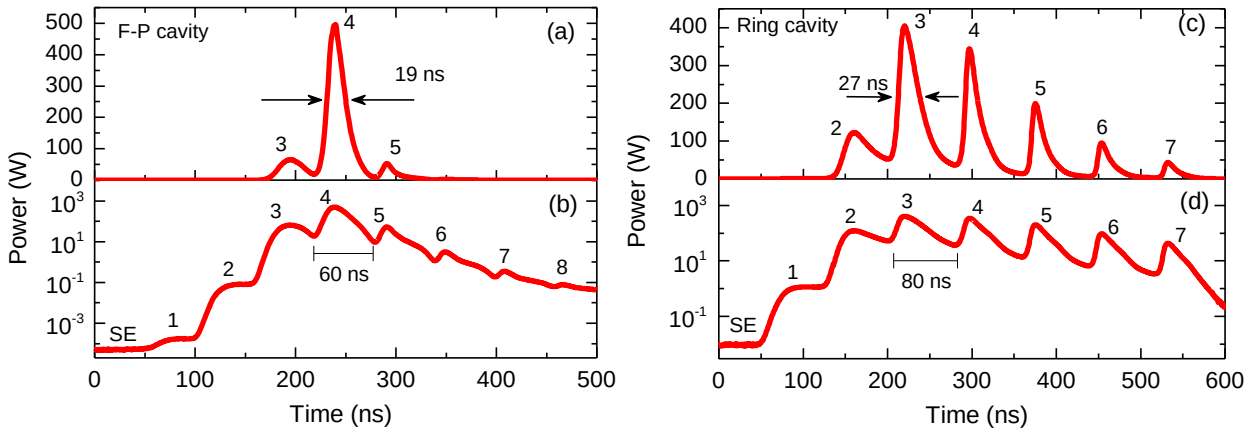

Figure 20. AQS pulses measured in (a) F-P and (b) ring FLs, with linear and logarithmic scales for both. Zero time corresponds to the moment when AOM is switched on. Numbers indicate the sequencing sub-pulses; SE marks the ASE level just before AOM opening.

3.3 Peculiarities of optical spectra measured for AQS pulses from F-P EDFL

Figure 21 shows the spectra of the AQS pulses registered from the F-P laser for different repetition frequencies, the CW state spectrum measured when the AOM1 was always in ON state is shown for comparison. As it is seen for repetition rates varied from 100 Hz to 2 kHz, the laser spectrum presents two sidebands arisen symmetrically on both sides of the laser wavelength. With increasing the AOM1 repetition rates in the interval of from 200 Hz to 2 kHz, the magnitude of these sidebands increases that is explained by increasing the averaged power of the pulses registered by OSA during the sampling interval. Then, from 2 kHz to 50 kHz sidebands' magnitude diminishes to some value below the ASE level (compare with the last spectrum measured for the laser operated in CW regime). The peak wavelengths of these two sidebands are marked by vertical dotted lines for Q-switch laser regime. Sidebands are positioned approximately at +13.4 nm and -12.6 nm from the laser wavelength, and equally spaced for repetition frequencies from 100 Hz to 5 kHz. The mechanism responsible for sidebands generation is attributed to the modulation instability (MI) effect that will be discussed in more details in Chapter 5.

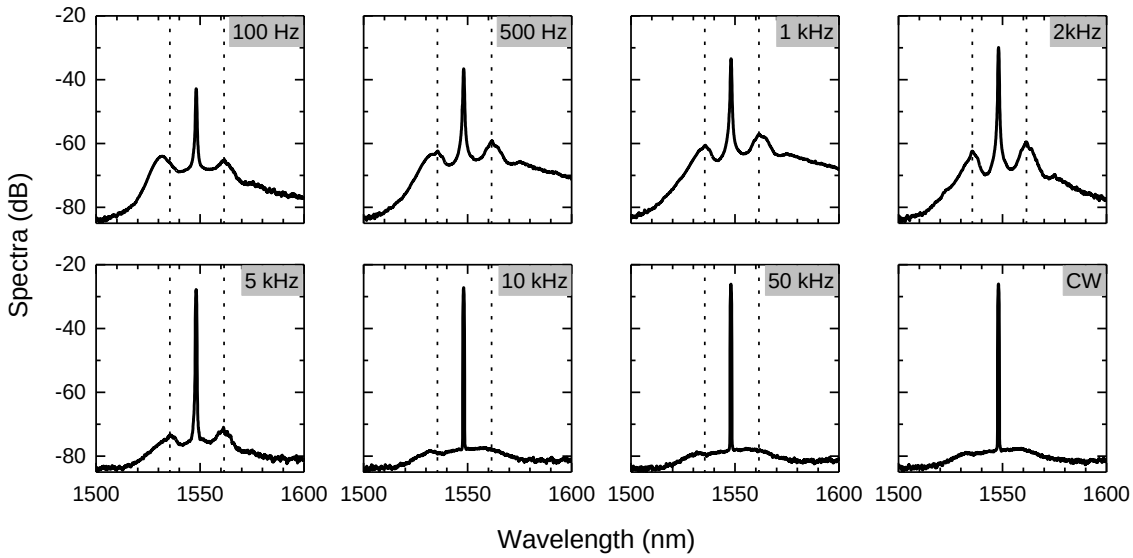

Figure 21. Pulse spectra versus repetition frequency in the F-P configuration. The vertical dote lines indicate the position of the sidebands for the Q-switch regime. The CW spectrum was measured keeping the AOM1 ON.

The proper laser line (peak at ~1548 nm) also spectrally broadened; this effect is exemplified in Figure 22 (a), where the optical spectra are shown at the same repetition frequencies as in Figure 21. The values of the spectral width measured at a 3-dB level for different repetition frequencies are presented in Figure 22 (b). Note that with increasing f_{rep} the laser spectral width tends to the spectral limit given by the continuous wave state. Also, note that a few spectral sideband ripples are observed at the long-wavelength slope of the laser line at repetition rates below 2 kHz. Thus, one can see that in F-P Q-switch laser, spectral broadening impacts the pulse spectrum when the optical field has a spectral bandwidth comparable to the bandwidth of the wavelength-selective reflectors (FBGs in our case) used in the laser cavity.

A similar effect has been recently observed in powerful ytterbium-doped QSLs (where laser spectra are overlaid on the output FBG reflection spectrum) [44], [45] and in watt-level mid-infrared QSLs [16].

In the literature, the line broadening discussed above results from self-phase modulation (SPM), which is induced in the long passive fiber tails of WDM2 and AOM2. Such spectral broadening will be discussed in Chapter 4 regarding the effective optical bandwidth and its influence on photon statistics, and SPM will be discussed in Chapter 5 the along with the nonlinear effects related to MI and Raman scattering.

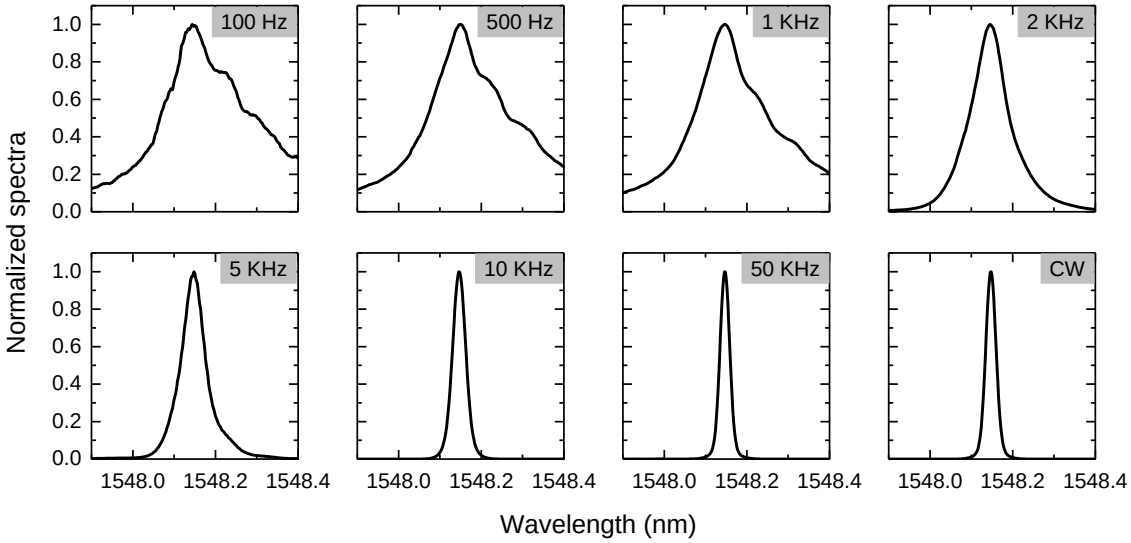

(a)

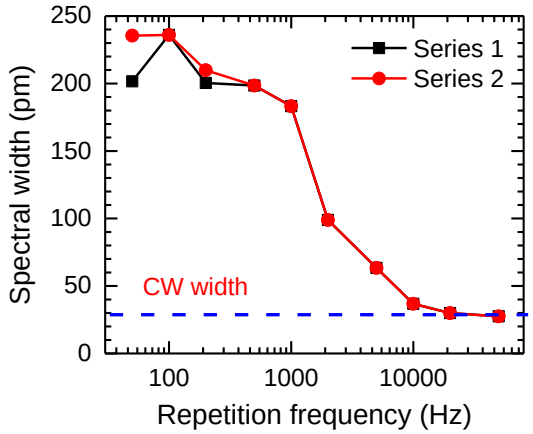

(b)

Figure 22. (a) Optical spectra of the mean sub-pulse for selected repetition rates and (b) its spectral widths measured at 3-dB level, all obtained for F-P AQSL. The AOM2 time gate was set to 28 ns (FWHM) and the OSA resolution was 20 pm.

3.4 Spectral dynamics of AQS pulses

The optical spectrum of pulses from both F-P and ring QSLs for 1 kHz are shown in Figure 23, where the AOM2 gate was set to 600 ns that permitted one to register all powerful sub-pulses of which the whole AQS pulse consists. The OSA resolution was set to 2 nm, therefore the linewidths of the sub-pulses spectra are overestimated. Note that similar spectra of AQS pulses from F-P laser were also observed by other authors, see ref. [18], however, no detailed explanation has been given yet for this detail. In addition, properties of the optical spectrum of AQS pulses from the laser with ring free-filter geometry have never been reported till now.

The spectra measured for AQS pulses from ring laser two spectral peaks, centered at 1530 nm and 1560 nm. These peaks do not resemble the transmission curve of 20:80% multiplexer used for laser output coupler (see Figure 16 (b)) and neither the transmission of any elements within the cavity. The peak at 1530 nm corresponds to the maximum gain (and therefore of ASE) of the strongly charged erbium-doped fiber whereas the peak at 1560 nm – to that of the partially charged one [19]. Note that from Figure 23 one cannot determine the spectral dynamics of the Q-switch pulse.

In order to study the spectral dynamics of AQS pulses from both the F-P and the ring lasers in details and also to understand how the pulse characteristics varies with AQS pulse evolution, we set another AOM (AOM2) at the laser output (see Figure 15), which permitted us to select the most powerful part of each sub-pulse shown in Figure 20.

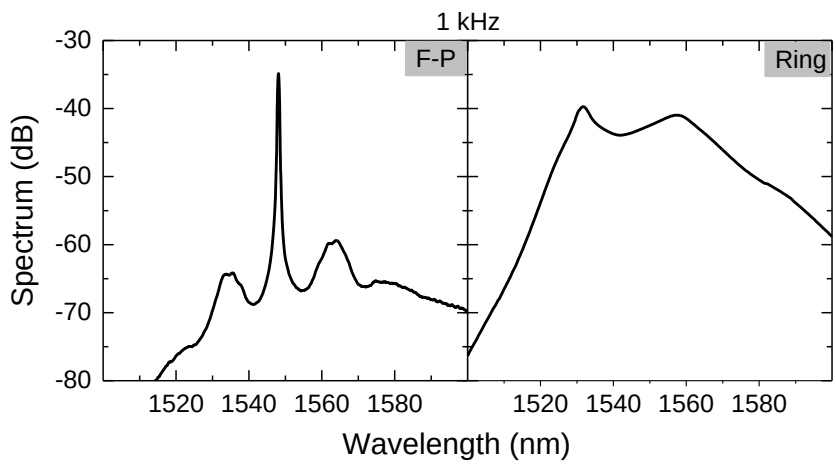

Figure 23. Optical spectra obtained at 1 kHz of AOM1 repetition frequency for FLs assembled in F-P (left) and ring (right) geometries. The AOM2 ON gate was set 600 ns.

The AOM2 was located outside the cavity, and it made possible to select the most powerful part of the desired sub-pulse and, at the same time at the same time AOM2 blocked the rest of AQS pulse. The selected part of the chosen sub-pulse is used for further analyzing. The extinction ratio from AOM2 (near to 3 dB) made it possible to measure only the first seven sub-pulses arising in the whole ASQ pulse train since the power of the sub-pulses with high number (>7) is comparable with the rest of power of the main sub-pulse propagating through the blocked AOM2. Even though to be able to measure the first and second sub-pulse we trimmed the amplitude of the subsequent sub-pulses.

The sub-pulse spectrum was measured separately by setting a transmission window of AOM2 to 28 ns at FWHM of either sub-pulse, then a delay interval had to be chosen to match the AOM2 trans-

mission's peak with the top of the selected sub-pulse. Note that the drivers of both AOMs were controlled by a multichannel pulse generator (*Stanford Research Systems*, DG645) with four synchronized outputs, all having a rise time of 800 ps. The AOM2 was followed by a variable attenuator (VA) used to maintain the registering electronics below saturation. As the delay of each sub-pulse with respect to the moment when AOM1 is switched ON (zero-time) is known, the delay of AOM2 gate can be easily chosen such that the latter modulator transmits light on a maximum of the selected sub-pulse. Then, by connecting the VA fiber output to OSA, we were capable of measuring separately optical spectra from each sub-pulse.

3.5 Features of the broadband optical spectra of pulses from F-P AQS EDFL

The sub-pulses' spectra captured from F-P laser after applying the procedure discussed above are illustrated in Figure 24. All the spectra are centered at 1548.14 nm (the wavelength selected by FBGs). Since the AQS F-P fiber laser is a multi-pass fiber amplifier of ASE (frequency shifted by 110 MHz on each pass through AOM1), all sub-pulses consist of ASE in the whole erbium range (it usually takes very small part of the whole laser signal) plus strongly amplified narrow-band ASE filtered by FBGs.

All sub-pulses contains two ASE portions: (*i*) the broadband (no filtered) ASE and (*ii*) the filtered ASE. A level of non-filtered ASE depends on EDF charge/gain and is formed by SE passed along the amplifying EDF to FBG1 for one time only (including the moment when AOM1 is OFF). Filtered ASE forms after reflecting by FBGs and amplification in EDF. Some reflections and amplification stages equal to the sub-pulse number.

The first sub-pulse consist of a portion of the broadband (no filtered) ASE whereas a portion of the filtered ASE is lesser; in all sub-pulses with number 2 and higher a portion of the broadband ASE is negligible. Therefore optical spectrum of the first sub-pulse presents a small narrow emission line superimposed above the strong pedestal of the broadband ASE.

As it is seen from Figure 24 for sub-pulses with numbers from 1 to 4, the level of the laser-line increases with its number, whereas for the next sub-pulses it decreases, the effect related to diminishing Er^{3+} population inversion level (EDF discharging); this evolution is also seen in the whole pulse shape (see Figure 20 (a)). In addition, for sub-pulses from 2nd to 7th, ASE level is almost below

the noise background of the OSA. The spectrum of fourth sub-pulse deserves special attention because of strong nonlinear broadening arising due to propagation along a relatively long (a few meters) passive fiber tails located between the active fiber and the VA. Nonlinear spectral broadening will be discussed in detail in Chapter 5. Finally, the spectrum marked as "Whole" in Figure 24 corresponds to one measured for the entire F-P pulse when the AOM2 gate was 600 ns. The "whole" spectrum is a superposition of all individual sub-pulses' spectra. For better comparison, the spectra of the whole pulse and the 4th sub-pulse are also shown in Figure 25.

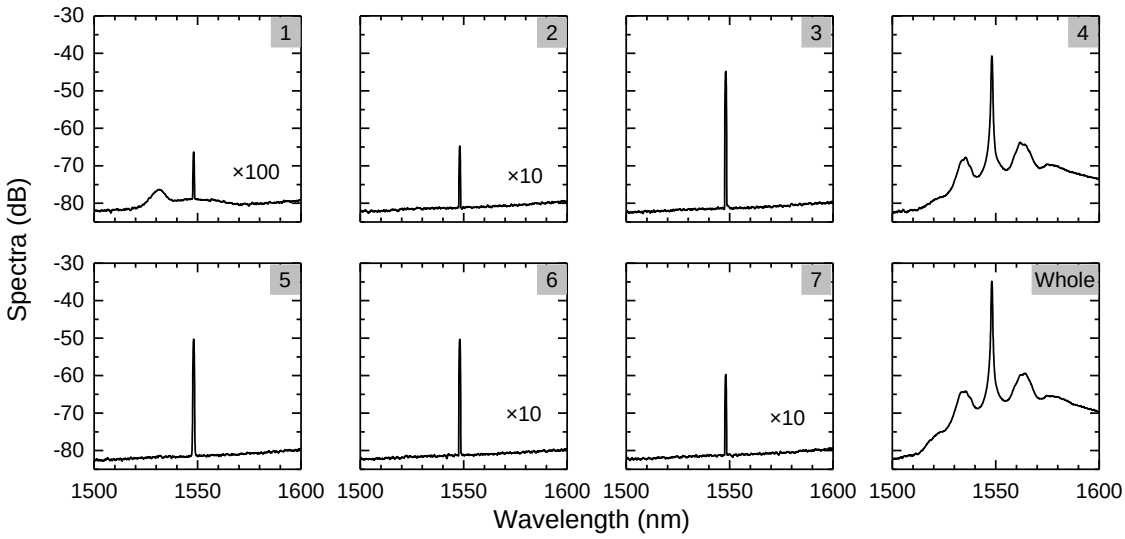

Figure 24. Spectra were measured for each sub-pulse separately using the AOM2 with gate of 28 ns; the sub-pulses' numbers are indicated in the right upper corners of correspondent panels. The spectrum of the "whole" pulse (the panel marked as "Whole") was obtained with the AOM2 gate of 500 ns. The attenuation was decreased for the 1st and the 2nd sub-pulses by 100 and 10 times, correspondingly.

A significant feature of the F-P QSL spectra is that sub-pulse fourth presents a much broader spectrum than other sub-pulses (see also Figure 21), with two broad sidebands arising from Modulation Instability (MI) [31], whereas spectra of others sub-pulses present only the main spectral peak. In addition, these sidebands are also presented in the whole AQS pulse spectrum measured at different repetition frequencies (see Figure 21 for frequencies from 50 Hz to 5 kHz), at which sub-pulses' power is more than 70 W, as can be inferred from Figure 19 (right) and Figure 21. MI and other nonlinear processes deserve special attention and will be retaken and discussed further in Chapter 5. The spectrum marked as "Whole" is a superposition of spectra of all sub-pulses. It can be seen that this spectrum is broadened to the longer wavelengths, up to 1700 nm, however the spectral broadening belongs only to the 4th (main) sub-pulse.

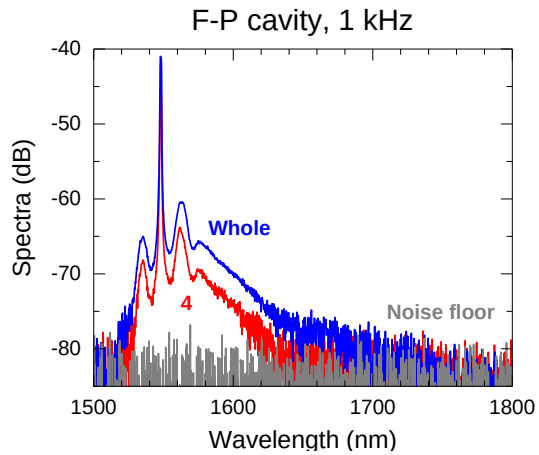

Figure 25. Spectra of the "whole" pulse and the 4th sub-pulse plotted in a wide spectral window.

3.6 Features of the broadband optical spectra obtained for pulses from ring AQS EDFL

In the ring AQSL all sub-pulses found in the whole AQS pulse are characterized by very broad optical spectra (see Figure 23 and Figure 26) due to the absence of spectrally-selective elements in the laser cavity, and also demonstrate different dynamics as compared to the case of the F-P laser. In this case, the sub-pulses' spectra move step by step to longer wavelengths with increasing the sup-pulse number, which results from the shift of the peak wavelength of EDF gain with decreasing Er^{3+} ions' inversion level [19].

The spectra of the first tree sub-pulses are centered near 1530 nm, the wavelength that corresponds to a spectral maximum of the gain of fully charged EDF (most of Er^{3+} ions are in the laser state), whereas the spectra of other sub-pulses are centered at approximately 1560 nm, that is a spectral maximum of partially discharged EDF [19]. Moreover, the spectra of the sub-pulses with numbers from 2 to 4 demonstrate two ASE peaks with different magnitudes; the ratio between them depends on the sub-pulse number and relates to inversion value of Er^{3+} ions: when the inversion level is lesser, the ASE peak at 1560 nm is more dominant.

The spectrum of the 3rd (most powerful) sub-pulse is most broader because during its developing a population inversion of Er^{3+} ions drops from the level at which a peak of EDF gain is at 1530 nm to the level characterized by the peak at 1560 nm; this rapid process (~30 μs, see Figure 20 (b)) is averaged by OSA with low measuring time (seconds). Spectra of the following sub-pulses, from 5th to 7th, get narrowed gradually around their peak wavelength, 1560 nm, and also decrease in their

width and spectral magnitude due to a significant depopulation of the Er^{3+} laser level. The curve marked as "Whole" was the spectrum of the entire AQS pulse from the ring laser when the AOM2 gate was 600 ns, which, indeed, is a superposition of spectrum of all sub-pulses appearing in the whole AQS pulse.

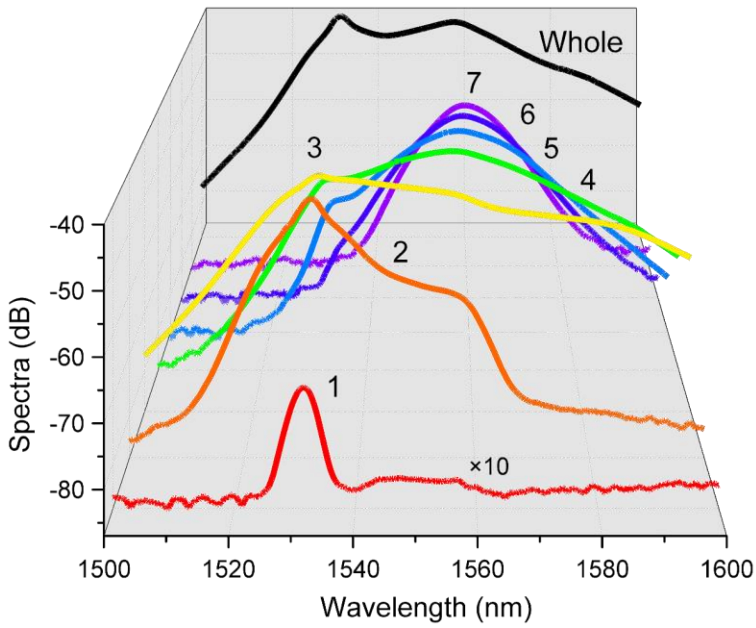

Figure 26. Optical spectra of sub-pulses measured from AQS EDFL assembled in the ring geometry. The sub-pulses' numbers are indicated near the correspondent curves. The spectrum named as "Whole" was measured for the whole AQS pulse when the AOM2 gate was 600 ns. The first sub-pulse was measured with VA attenuation decreased by 10 dB.

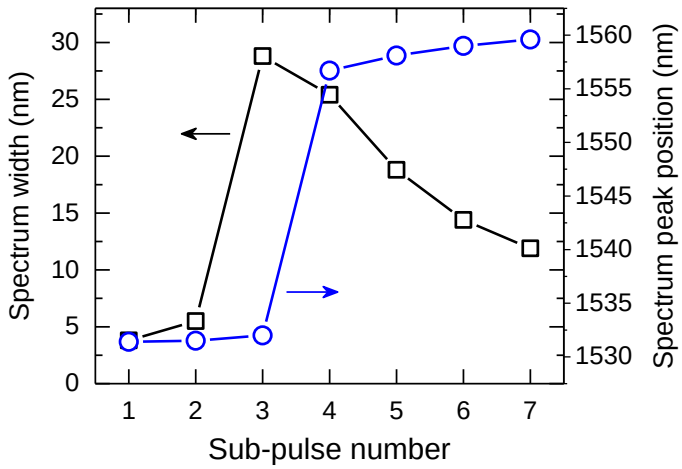

Figure 27. Spectrum width (curve 1) and its peak position (curve 2) versus the sub-pulse number.

Dependences of the width of sub-pulses' spectra were measured at 3-dB level each, and their peak wavelengths are demonstrated as a function of the sub-pulse number in Figure 27. It is seen that the spectrum of the most powerful sub-pulse (the 3rd) is broader by approximately seven times as

compared to the first two sub-pulses (it varies from ~4 nm to ~30 nm). Starting with the third sub-pulse, the spectrum width smoothly decreases down to ~ 11 nm for the 7th sub-pulse (the last one in the series under study).

3.7 Features of the narrow-band optical spectra of pulses from F-P AQS EDFL

We have discussed above the spectral characteristics of F-P and ring Q-switched fiber laser for a broad wavelength range, from 1500nm to 1600 nm. Nevertheless, a spectral dynamics observed in a narrow wavelength range deserves special attention for AQS pulses from the F-P EDFL. The experimental and simulated results regarding spectral broadening are shown in Figure 28 in a narrow wavelength range (from 1548.0 nm to 1548.3 nm). The spectra were measured using OSA with a spectral resolution of 20 pm. In each panel of Figure 28 the spectra of (i) reflection of the output coupler FBG1 as it is, (ii) the experimental spectra of sub-pulses, and also (iii) the simulated function $F(n,\lambda)$ of the spectrum of the output laser signal after n passes of the laser wave along the cavity (i.e. for n-th sub-pulse) in absence of nonlinear effects, which is found as follows:

$$F(n,\lambda) = \left[R_1(\lambda) R_2(\lambda)\right]^n T_1(\lambda), \tag{14}$$

where $R_1(\lambda)$ and $R_2(\lambda)$ are the FBGs wavelength dependent reflections from FBG1 and FBG2, respectively. $T_1(\lambda)$ is the FBG1 transmission and n is the sub-pulses number, which is equal to the number of ASE round-trips in F-P geometry. As can be seen from Figure 28, the spectra of the first three sub-pulses are well fitted by eq. (14), with a small deviation arising for the third sub-pulse spectrum from the modeled one; see also Figure 29 where 3-dB widths of the spectra of all sub-pulses measured separately and of the whole AQS pulse are presented.

From these two figures, one can see that the spectral width of the main sub-pulse (#4) is by ~3.5 times wider than the one modeled by eq. (14). The spectra of the following 5th to 7th sub-pulses demonstrate narrowing with increasing their number, but they are always broader than the modeled ones. Furthermore, starting from the 6th sub-pulse, sub-pulses becomes narrower than the output FBG spectrum (refer to Figure 16). Moreover, the spectrum of the whole AQS pulse, measured at AOM2 gate of 600ns (see the panel labeled as “whole AQS pulse” in Figure 28), is broader than the output FBG1 spectrum due to strong contribution of the 4th sub-pulse.

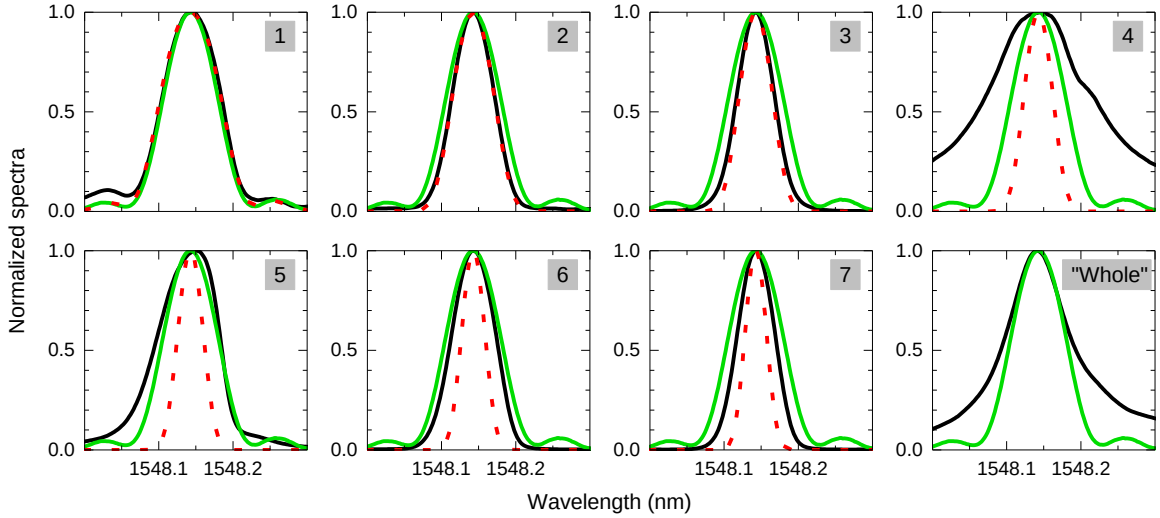

Figure 28. Narrow-band optical spectra of consequent sub-pulses from F-P AQS presented in linear scale. Experimental data are shown by solid black curves, fit using eq. (14) are represented by the red dashed curves. For comparison, a reflection spectrum of FBG1 is also demonstrated (by green curves). The sub-pulses numbers are indicated in each window. OSA resolution was set to 20 p.

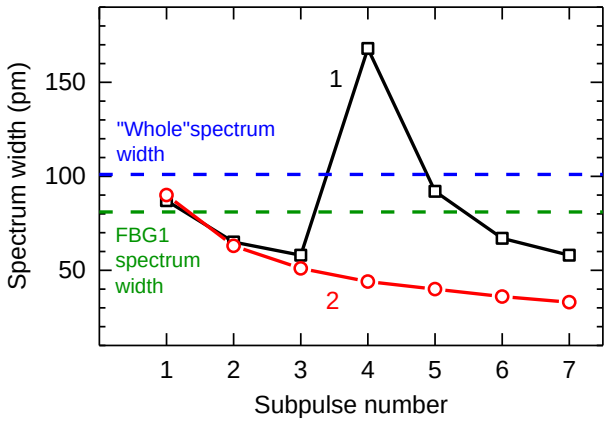

Figure 29. Spectral width of sub-pulses as a function of their number. The curves 1 and 2 show the experimental data and the simulation results using eq. (14), correspondingly. The horizontal dash lines designate the spectral widths of FBG1 coupler (green dashed line) and the whole AQS pulse (blue dashed line), respectively.

3.8 Study of supercontinuous generation using pulses from F-P and ring AQS EDFLs

The next part of the experimental investigation was focused on the study of supercontinuous generation in a standard communication fiber using AQS pulses from the fiber lasers under study. For this aim, a 100-m long SMF-28 communication fiber (passive fiber) was spliced to the outputs of each AQS EDFL (to the lower output of WDM2 in the case of F-P laser or 80% output of 20:80 multiplexer for the ring laser, see Figure 1).

Profiles of the pulses entering the passive fiber are shown in Figure 30 by the black lines, while the profiles of ones measured on the passive fiber output are demonstrated by the red lines. As it is seen, due to nonlinear effects responsible for supercontinuum generation a portion of the powerful sub-pulses is depleted, keeping only wings of the sub-pulse behind. The sub-pulses with a peak power less than 100 W are not deformed.

Pulse depletion of this form is understood in the context of spontaneous Raman buildup [46], [47] and results from the intensity dependence of the Raman gain and the fiber length. However, measurements show a discrepancy with simulations, since the central part of the pulse is not fully depleted while in the simulation it is always depleted for the same fiber lengths. It is worth mentioning that the wavelength dependence of the photodetector response decays linearly from its maximum 100% at 1600 nm to 20% at 1700 nm, so important portion of the Raman signal is also detected therefore diminishing the “hole” deep in the centers of the most powerful sub-pulses.

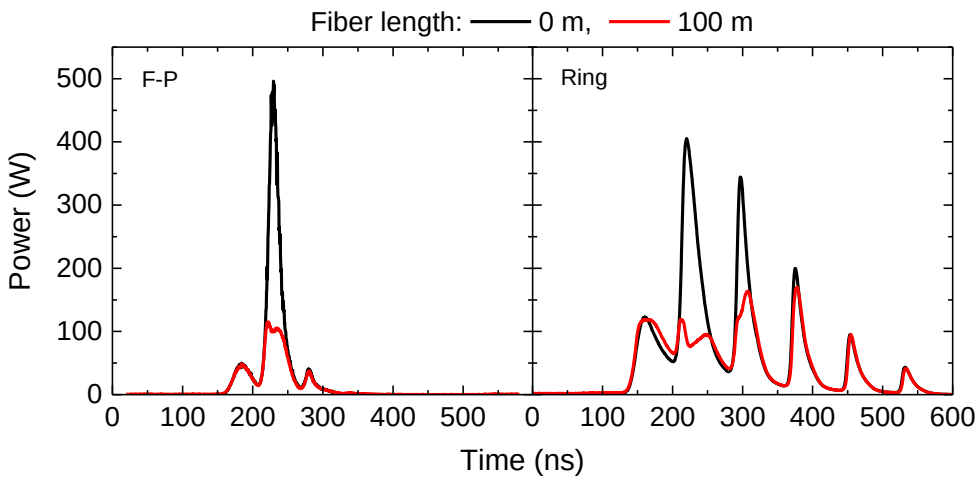

Figure 30. Pulse profiles obtained for repetition rate of 1 kHz. The black line shows the shapes of the pulses at the passive fiber input whereas the red lines correspond to the pulses after 100-m long fiber. In these, the cases averaging by 100 realizations was applied.

The following Figure 31 illustrates the supercontinuum spectra measured on the output of the passive fiber spliced with the output of either laser. The spectra were obtained by the OSA with the wavelengths’ range from 1200 nm to 2400 nm for the AOM1 gate of 600 ns at which the “whole” AQS pulses enter the passive fiber. These spectra are the superposition of supercontinuum generated by each sub-pulse composing the “whole” AQS pulse. Examples of the partial supercontinuum spectra obtained separately for powerful sub-pulses after temporal gating by AOM2, placed after the passive

fiber, are shown in insets. Note that since the transmission of AOM2 designed for 1060 nm is spectrally depended, the supercontinuum spectra measured for different sub-pulses are convolutions of the real spectra and the AOM2 transmission spectra.

From the inset of the left window (F-P cavity), one can see that the spectra of the 3rd and 5th sub-pulses are broadened similarly, with some difference in magnitude. Supercontinuum generated by the 4th sub-pulse experiences the broadest bandwidth and the strongest spectral density, which contributes with the highest weight to the "whole" spectrum reaching 2200 nm. It also modifies the spectral position of the sidebands discussed above. In contrast, the spectral broadening obtained using AQS pulses from the ring laser arises mainly from the 3rd sup-pulse, its spectrum is limited by 1950 nm. The 4th sub-pulse contributes with the strong spectral peaks at 1560nm and 1670 nm. The excessive noise in supercontinuum spectra observed near 1850 nm results from water absorption [48].

The nonlinear optical effects involved in the generation of new spectral components resulting in supercontinuum generation will be discussed in details in Chapter 5.

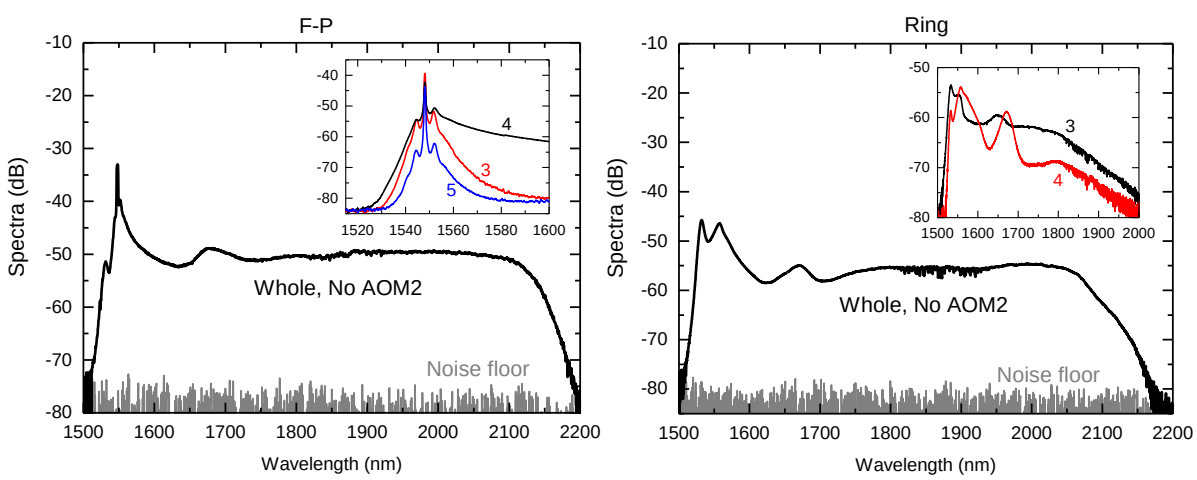

Figure 31. Optical spectra generated by the whole AQS pulses measured after 100 m passive fiber for F-P (left) and ring (right) lasers. Inset to the left window (F-P laser) shows the partial spectra generated by the 3rd, the 4th, and the 5th sub-pulses, whereas the inset to the right window (ring laser) shows the spectra generated by the 3rd and the 4th sub-pulses.

Chapter 4 Temporal Noise Dynamics

Active Q-switched laser pulsing is not a *per se* stable process, it demonstrates timing and amplitude jitters that depends on laser parameters as the active fiber length, cavity losses, pump level. [49]. Undesired fast intensity instabilities observed usually in AQS pulses are often attributed to ASE noise, see, for example, ref. [18], but its statistics dependent on ASE optical bandwidth has never been studied. In this chapter, we found important to analyze the effect of the ASE bandwidth on a level of intensity fluctuations (photon statistics) in AQS pulses, which permits one to understand deeper the physical processes behind AQS pulsing.

4.1 Experimental arrangement

We analyzed intensity noise of pulses from the F-P and the ring AQS-FLs (see Figure 15 for experimental arrangements) measured in time-domain using 4.5 GHz photodetector and 3.5 GHz oscilloscope. This study was motivated by the observation of a very high noise level encountered in AQS pulses as it was discussed above. Since the F-P and the ring FLs are the most common ones, the noise properties of pulses obtained from these two types of lasers were studied for these two laser types, including dependence of noise on optical bandwidth. Our measurements were limited by the response time of available electronics, such as the oscilloscope, photodetectors, RF cables, *etc.*

Figure 32 illustrates two examples of typical single-shot scans of the AQS pulses from the F-P FL, both were measured at the same sampling rate of 40 GS/s but with different photodetector RF bandwidths (BW) (1 GHz and 4.5 GHz). It is seen that the number of the detected noise spikes per subpulse and also the range of intensity fluctuations grow with increasing RF band. Thus, one can conclude that slow detecting devices do not allow a correct study of the noise statistics in AQS pulses; in the ideal case, the RF bands of photoreceiver and oscilloscope used in experiments should be equal or at least comparable to the optical band of the optical signal whose statistics is under study. In our

case, the RF bandwidth of the detection scheme based on 4.5 GHz photodetector and 3.5 GHz oscilloscope was limited by the oscilloscope band corresponding to ≈ 30 pm band of the optical signal, which is comparable to the optical band of AQS pulses from F-P FL (see discussion in Chapter 3). Note also that the oscilloscope bandwidth will be taken below as the "PD-counting time" (T).

A remarkable effect relating to the AQS pulses is that the intensity fluctuations differ from pulse to pulse, showing the stochastic nature of ASE fluctuations. Since the optical shift in the AOM used for modulating Q-factor of FL cavity (220 MHz per photon round trip in cavity) differs from the mode-beating frequency (≈ 16.7 MHz) and its harmonics, the AQS pulsing under study is not "classic" lasing arising at the cavity modes but instead it is incoherent random ASE spiking or so-called "bunching" effect.

Although the pulses shown in Figure 32 were measured for the time interval corresponding to the whole AQS pulses obtained at the repetition frequency of 1 kHz, only 4th sub-pulse can be seen due to its high peak power. Note also that the repetition rate of 1 kHz was chosen due to reasons discussed in Section 3.3.

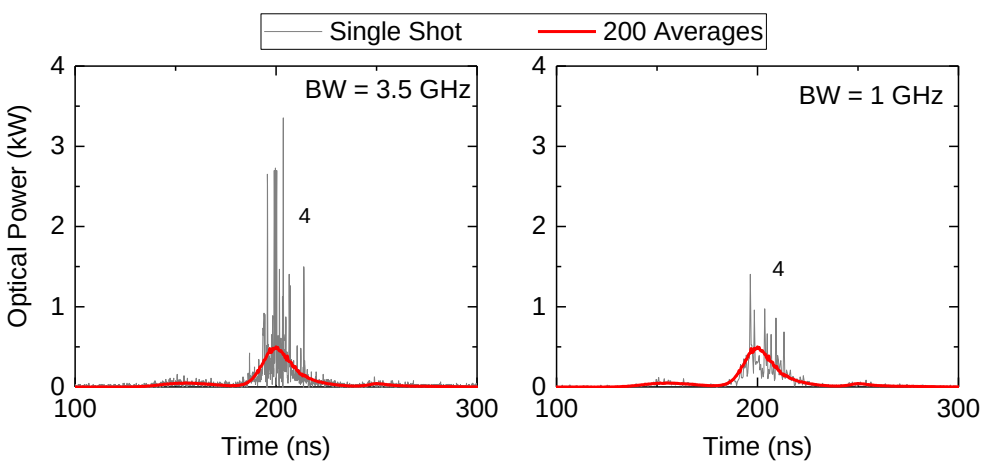

Figure 32. Typical single-shot scans of AQS pulse (grey lines) for F-P laser configuration. The scans were obtained using two photodetectors with different bandwidths (BW): 4.5 GHz (left figure) and 1 GHz (right figure), at the same oscilloscope with RF band of 3.5 GHz and a sampling rate of 40 GS/s. The red lines show pulses averaged over 200 samples. "Zero time" was determined as the moment when AOM1 was switched ON.

Further support for this hypothesis was noise properties of ASE filtered by an FBG1. In this experiment, ASE filtered by FBG1 was measured at AOM's "0" order output via circulator as is illustrated in Figure 33 (a). Additional FBG connected to the circulator was mechanically tuned to move its peak wavelength that of FBG1 and was used for rejecting the broadband ASE from EDF. Noise signal

of narrow-band ASE, shown in Figure 33 (b), was detected after reflection by FBG and passing through an optical circulator. The histogram of the intensity distribution is then reported in Figure 33 (c). It can be seen that the histogram is asymmetrical with longer right tail corresponding to rare high-intensity events; such effect is typical for narrow-band spontaneous emission.

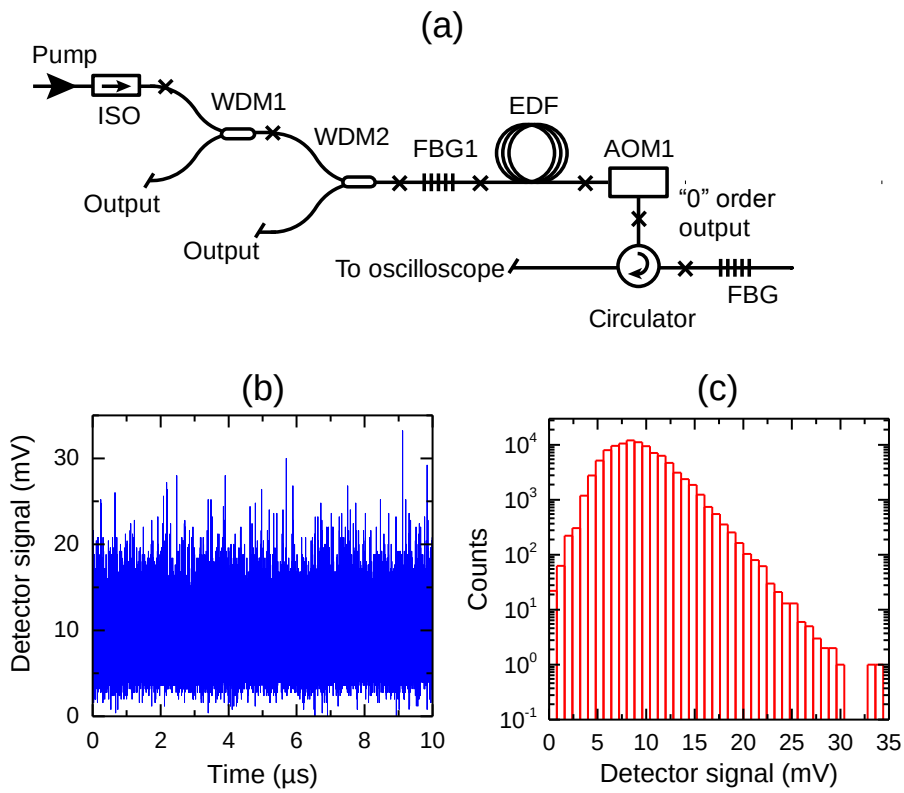

Figure 33. (a) Experimental set-up for detecting the ASE spiking. (b) Time-domain experimental measurement is shown a chaotic behavior of ASE spiking. (c) Probability histogram obtained for the process shown in (b).

Figure 34 presents the typical single-shot waveform of QS pulse obtained from the ring AQS EDFL using the same detection arrangement as in the case of the F-P laser discussed above: 4.5 GHz photoreceiver at a sampling rate of 40 GS/s (gray line), and its averaged waveform over 200 scans (red line). Comparing the results shown in Figure 32 and Figure 34, one can see that the AQS pulses produced by FL with a F-P cavity (Figure 32) are tremendously noisy, with some peaks of noise power greater by an order of magnitude than the mean pulse power, whereas noise component of pulses released from the laser with the ring cavity (Figure 34) is with essentially smaller magnitude, not exceeding several percents of the mean pulse power.

The main difference between the pulses measured from F-P and ring AQS FLs resides in their optical bandwidth which is by two to three orders broader in the case of the ring cavity as compared

to the case of the F-P cavity. In spite of the intensity fluctuations (arising from ASE) are really of the same order of magnitude for both laser realizations, the fluctuations characterizing pulses from the ring laser are too rapid for direct detecting. In the latter case, the high-frequency spectral components of the fluctuations (above 3.5 GHz in our case) are cut off by the measuring set photodetector/oscilloscope acting as the short-pass RF filter with a cut-off at 3.5 GHz.

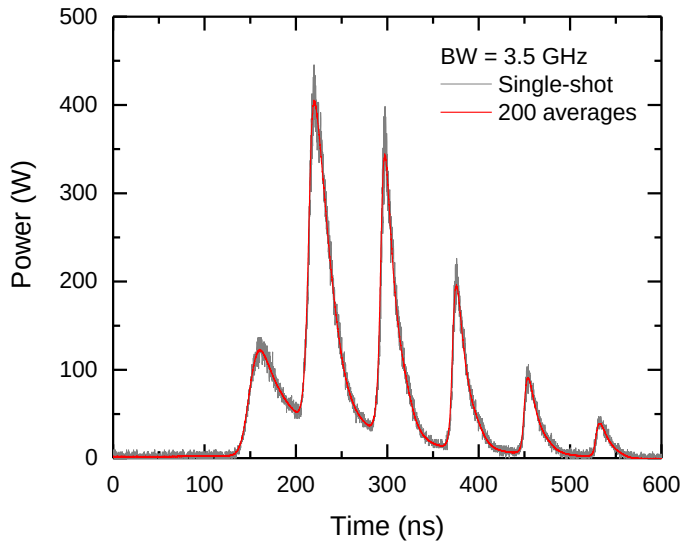

Figure 34. Typical single-shot trace of QS pulse obtained from the ring AQS EDFL (grey line) and the signal obtained after averaging by 200 realizations (red line). RF bands of the photodetector and the oscilloscope used were 4.5 GHz and 3.5 GHz, correspondingly. The oscilloscope sampling rate was 40 GS/s.

Before analyzing the noisy signals, a detail calibration of the sub-pulses mean power and the time of arising were performed. Typical oscilloscope traces of the pulses measured at 1-kHz repetition rate and averaged over 200 realizations are shown in Figure 35 (a) for the F-P laser and in Figure 35 (b) for the ring laser, both in logarithmic scale. It is seen that the pulses are composed of a few sub-pulses, starting from broad-band ASE arising when AOM1 is still OFF (labeled by “0”) (see also Figure 15 for the lasers’ setups). Note that the same traces but plotted in linear scale are shown in Figure 32 (F-P cavity) and Figure 34 (ring cavity), along with the noise pattern of pulses. Since power of the sub-pulses scales in very broad range (from 300 μW to ~ 0.5 kW), the whole AQS pulses were obtained by measuring separately either sub-pulse using AOM2, turned to different transparencies gates and different delays from zero time, and varying VA transmission to adjust power at the PD input and, finally, adjoining the data obtained.

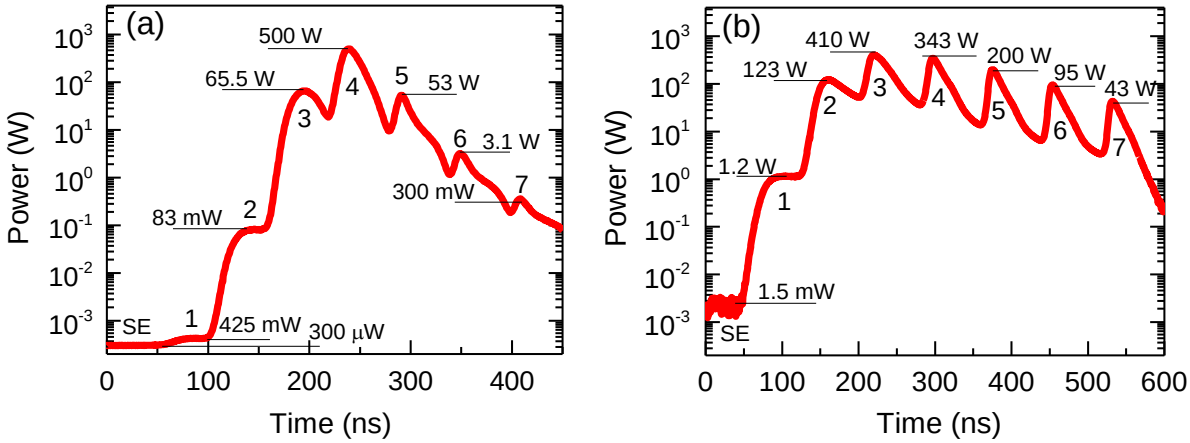

Figure 35. AQS pulses measured from (a) F-P and (b) ring EDFLs. Numbers indicate the sequencing sub-pulses; the ASE level just before AOM1's opening is marked by "0" (zero time corresponds to the moment when AOM1 is switched on). The averaged peak sub-pulses' power is indicated above each sub-pulse. In both laser configuratios, the repetition rate of AQS pulses was 1 kHz.

4.2 Photon noise distribution

In this section, it will be discussed the results of measuring the photon probability distribution (PPD) relating to intensity noise for each sub-pulse of which the whole AQS pulse consists, first at the output of AQSL. Then, the PND was measured after 100 m of a single-mode passive fiber (SMF-28) connected to the laser output, with the same averaged peak powers of the sub-pulses as it was used for measuring PND at the AQSL output. The passive fiber was used here as a nonlinear medium with anomalous dispersion. The measurement of PND after the long fiber allowed us to determine the impact of new spectral components generated along the nonlinear fiber on the photon distribution.

In this study, the mean power of each sub-pulse on the PD's entrance was set to 20 μW and 60 μW for EDFLs with F-P and ring cavity, respectively, ensuring an unsaturated PD regime at measuring noisy signals. Note that, in both cases, the mean power was much higher than ~ 1 μW of noise equivalent power (NEP) of the PD in the whole RF bandwidth.

Figure 36 demonstrates an oscilloscope screen-shot in which a procedure of typical a standard measurement of the intensity fluctuations for different sub-pulses is illustrated. The histograms of the intensity fluctuations that are proportional to photon noise were recorded using the "Waveform Histogram Lab" (WHL) program (a software tool inside the firmware of the oscilloscope in standard configuration). The WHL digitizes the photodetector signal to 255 bin values, then summarize these

counts, and finally displays the histogram on the left vertical axis of the screen (see Figure 36). Also the histogram can be saved in a text file for further analyzing.

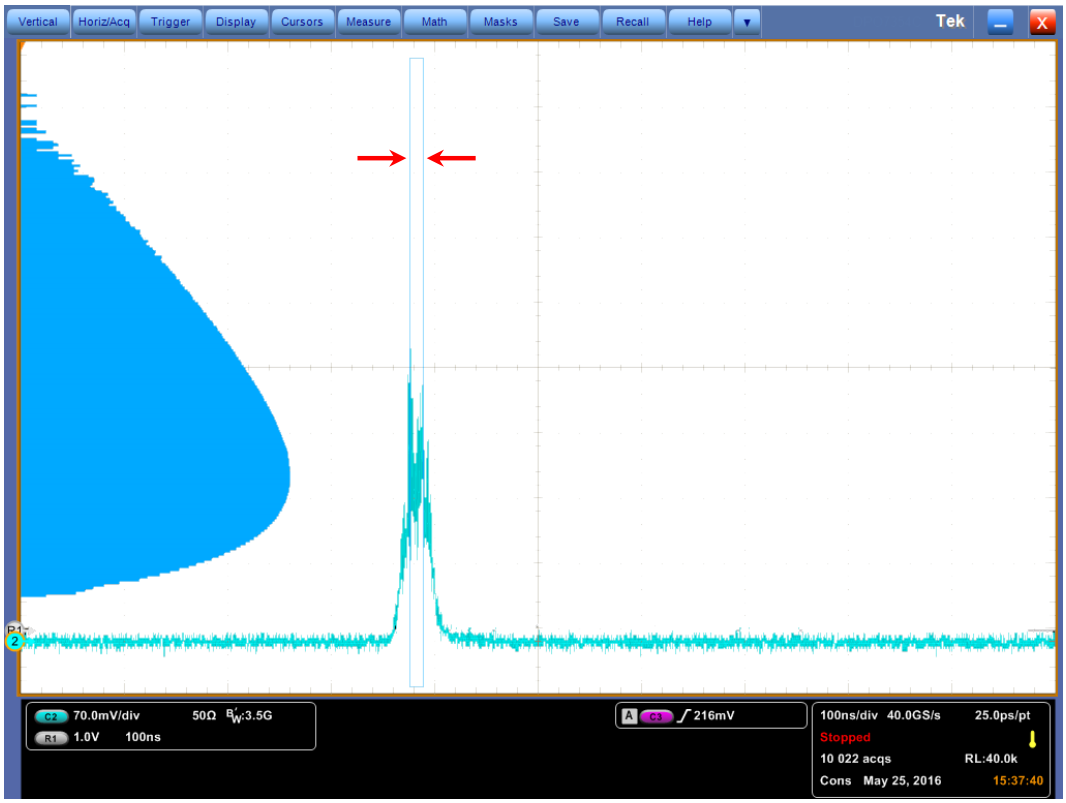

Figure 36. Screen-shot showing a typical measurement of the amplitude oscillations. The histogram magnitude (photon count) in log scale is displayed on the left vertical axis. The red arrows show the interval of photon counting.

To study the photon statistics separately for each sub-pulse, the AOM2 gate was moved to a maximum of a selected sub-pulse while the PD signal was counted within a short interval, $\Delta t = 2$ ns, during which the mean signal on the top of the chosen sub-pulse did not change. To get a smooth histogram of the photon distribution, the data were acquired and cumulated over 10^4 realizations, corresponding to the overall counting of 20 µs.

As mentioned above, the mean power at the PD entrance was fixed at 20 µW for each sub-pulse under study, which corresponds approximately to 4.5×10^4 photons, caught within the counting interval of the PD ($T \approx 300$ ps).

4.2.1 Photon Statistics in the F-P Configuration: Bose-Einstein Distribution

In Figure 37, we show two series of experimental PPDs measured on the F-P EDFL's output in the cases when (*i*) the broadband ASE signal was measured (before AOM1 switching ON), which is

presented in the top-left panel marked as "SE" (see Figure 35 (a)), and when (*ii*) all the sub-pulses, from the first to the seventh ones (see the rest of panels) that were composed of ASE with much narrow optical band. The first series of PPD (shown by black stars) corresponds to the PD signal measured at the laser output and normalized to their most probable value (NPPD). The second series (shown by blue circles) corresponds NPPD measured on the output of 100-m SMF-28 fiber (passive fiber), connected to the EDFL output. It demonstrates the features of noise statistics resulting from the interaction of powerful-noisy AQS pulses with the long passive fiber with anomalous dispersion.

The solid red lines represent the best fits of NPPD, obtained using eq. (12) for broadband ASE registered before AOM1 switching ON and using eq. (10) for sub-pulses registered after AOM1 switching ON. The parameters obtained by fitting the photon distributions were the mean number of photons $\bar{n}$, in the case of ASE acquired before AOM1's switching ON, or the mode numbers M_{BE} for the sub-pulses. To facilitate numerical simulations for statistics of sub-pulses, we used the mean photons' numbers equal to $\bar{n} = 10^4$. Remember that the normalized Bose-Einstein distribution does not depend on the photon number when it equals to or higher than 10^3 (see Section 2.3).

It is seen that the noise signal adherent to broad-band ASE before AOM1 switching ON (marked as "SE" in Figure 37) is described by Poissonian distribution with the mean photon number $\bar{n} = 510$ (corresponding to $M_p = 88$ from which the ASE effective bandwidth is estimated to be 12 nm). In turn, the photon distribution for sub-pulses with numbers 2 and larger are well fitted by Bose-Einstein distribution with M_{BE} varied from one sub-pulse to another. Despite sub-pulse 1 is a mixture of Poissonian and Bose-Einstein photons with a slight difference in mean powers, the photon statistics can be described as a BE distribution with a high number of modes ($M_{BE} = 16$) which gives an effective bandwidth of ≈ 210 pm, greater than the FBGs bandwidth (see Figure 29).

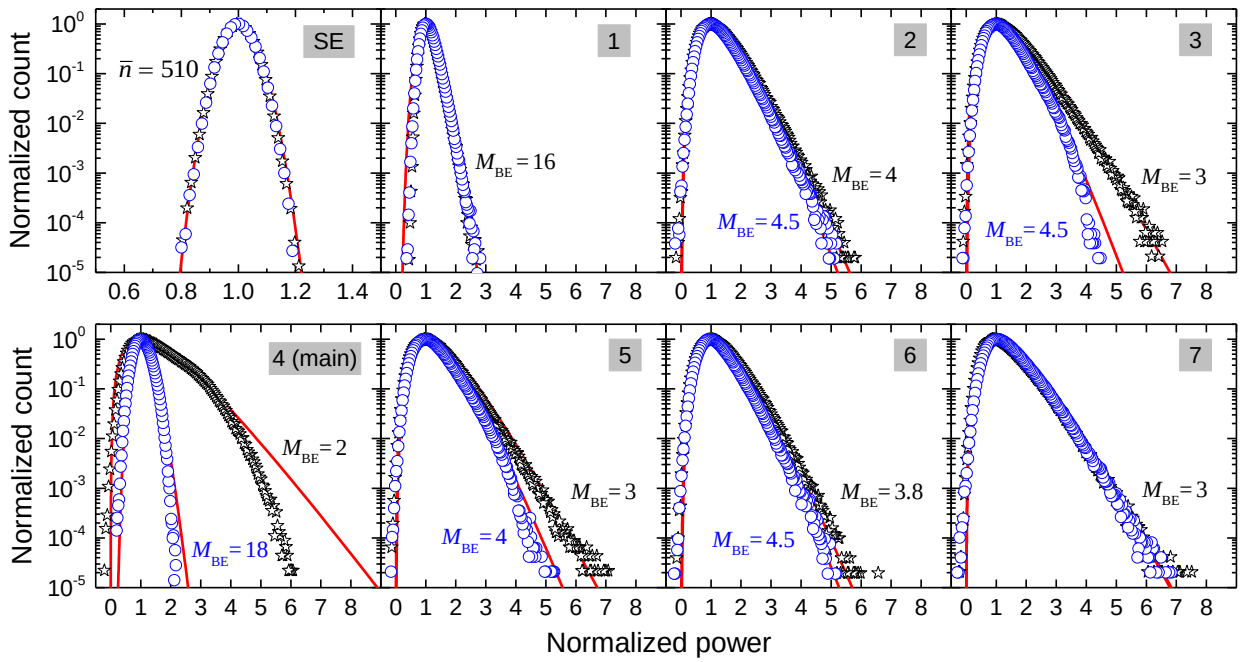

Figure 37. Normalized photon distributions obtained for broad-band ASE at closed AOM1 (the top-left window, marked as SE) and for different sub-pulses observed within AQS pulse for F-P EDFL (the rest of the windows). Each window shows two kinds of histograms: measured directly at the laser output (black stars) and after 100-m SMF-28 fiber, connected to the laser output (blue circles). The red curves are fits by Poissonian distribution for broadband ASE photons and by Bose-Einstein distributions with different M_{BE} for different sub-pulses.

The phenomenon of mode number variation stems from the two effects involved and acting simultaneously:

- The first of them is the narrowing of optical spectra (relating linearly to B_{BE}), in each consequent sub-pulse resulted from each subsequent reflection of ASE wave from FBG1 with narrow reflection spectrum, as it is shown in the previous chapter. This leads to decreasing the spectrum width and therefore the mode number. As can be seen from Figure 37, the mode number decreases up to 4th sub-pulse that presents spectral broadening due to SPM and MI, and also by increasing the spectral width of the following sub-pulses. Then the tendency of the spectrum width decreasing continues from sixth to seventh sub-pulse due to the subsequent spectrum narrowing by the output selective reflector FBG1.
- The second effect, but pronounceable in the above-mentioned most powerful sub-pulse (number 4), appears due to self-phase modulation (SPM) accompanied by spontaneous modulation instability (MI) [50], [51]. At this stage, the 4th sub-pulse undergoes spectral

broadening and transfers its energy to the new spectral components of the MI side-bands. Despite SPM does not affect the peak power of the noise spikes, MI depletes the most powerful spikes, which modifies the right-hand side of the NPPD (compare the experimental data shown by the black star symbols and the solid red line presenting the theoretical fit in Figure 35, the left bottom window). Note that NPPD measured for this sub-pulse, but after propagating along 100 m SMF-28 fiber strongly, differs from that measured on the laser output, the effect observed due to broadening the optical spectra (the mode number increases) by nonlinear effects in a long fiber.

NPPDs measured for the sub-pulses 3th and 5th are not distorted when measured on the laser output but demonstrated some cut of most powerful events when measured after the long passive fiber. It is also important to stress that these sub-pulses present small effect of MI in their optical spectra in accordance with the MI depletion phenomenon (see Figure 31) [50], [51]. No "cuts" in the histograms' tails are observed for less intense sub-pulses as well as for ASE detected before AOM1 switching ON, all measured at the AQSL output.

We will discuss nonlinear phenomena in details in section in Chapter 5 below, namely effects of the self-phase modulation (SPM) and modulation instability (MI) on AQS pulses' spectra.

The waveforms of F-P AQSL pulses measured at the output of the laser (marked as "0 m") and after 100 m of SMF-28 fiber are shown in Figure 38 (a) and Figure 38 (b), where the averaged AQS pulse (the red line) is superimposed to a typical single-shot scan (the grey line). Also, for a better comparison, the averaged waveforms captured at 0 m and 100 m are illustrated in Figure 38 (c). It is seen that the fluctuations of the main peak underwent depletion up to a level of ~ 100 W resulting in the NPPD deformation as it is shown in Figure 37 (see sub-pulses 3, 4, and 5). Other sub-pulses does not change in averaged power, but their noise distributions were still affected by small nonlinear interaction with the optical fiber resulting in slight decreasing the histogram widths, which corresponds to small increasing the mode numbers (see the changes in mode numbers in Figure 37 after propagation 100 m of the passive fiber).

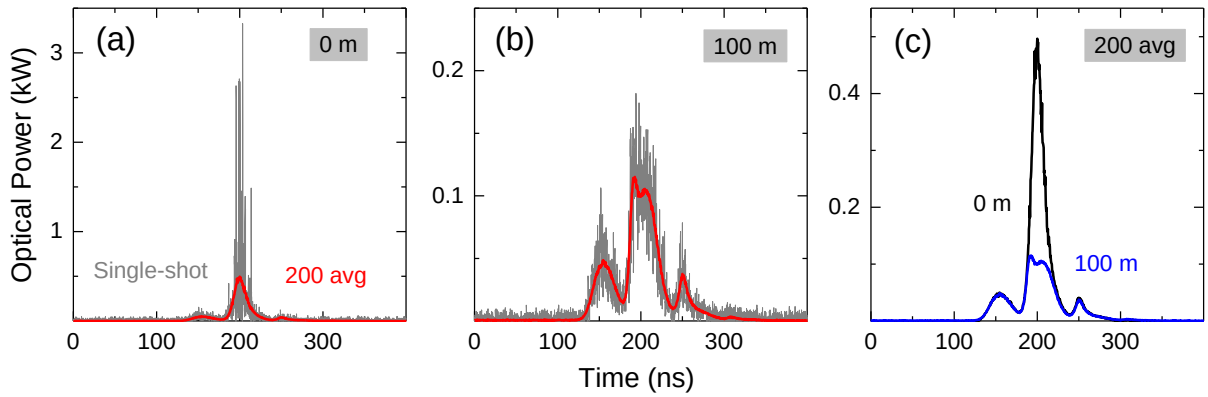

Figure 38. (a) and (b) Oscilloscope traces of averaged (red curves) and single-shot (grey curves) AQS pulses measured from F-P FLs. Traces are shown in (a) and (b) correspond to the pulses measured on the laser output and after 100 m of SMF-28 fiber, respectively. (c) Shapes of averaged AQS pulse measured on FL output (black line) and after 100 m of SMF-28 fiber (blue line).

4.2.2 Photon Statistics in the Ring Laser Configuration: Poisson Distribution

Figure 39 demonstrates the NPPD obtained for AQS pulses released from the EDFL in ring geometry, directly on the laser output and after the 100-m SMF-28 fiber connected to the laser output. Similarly to the case of the AQS EDFL with the F-P cavity discussed above, AOM2 was used for selecting PD signals adherent to different sub-pulses while optical power at the PD entrance was as well fixed but now at $W = 60$ μW, which equals to $\approx 1.35\times10^5$ photons falling into the PD counting interval T. From this figure, it is seen that the experimental noise histograms (see black stars that correspond to the photon distribution measured on the laser output) are well fitted by Poissonian distributions (see solid red lines). The number of photons per mode used in fitting determines the mode number, M_p, the latter inversely depends on $\bar{n}$ as it is seen in Section 2.3.

The NPPD of ASE measured before AOM1 switching ON (shown in the top-left panel of Figure 39), is well fitted by Poissonian distribution, as in the case of the F-P EDFL (see Figure 37), but now the photon number per mode is 1170 that corresponds to $M_p = 115$. This mode number yields an ASE effective bandwidth of 16 nm that is slightly bigger than the bandwidth characterizing ASE from the EDFL with F-P geometry before AOM1 opening (the ASE effective bandwidth was 12 nm). This difference apparently arises from the presence of spectrally selective WDM at the F-P laser output (compare Figure 15 (a) and Figure 15 (b)), which causes in the reduction of the ASE spectrum width. Furthermore, the Poissonian distribution for the powerful sub-pulses, from the first to fifth, are well fit-

ted with smaller mean numbers of photons $\bar{n}$ (or greater mode number M_P) and, correspondingly, larger EDFL's linewidth B_P.

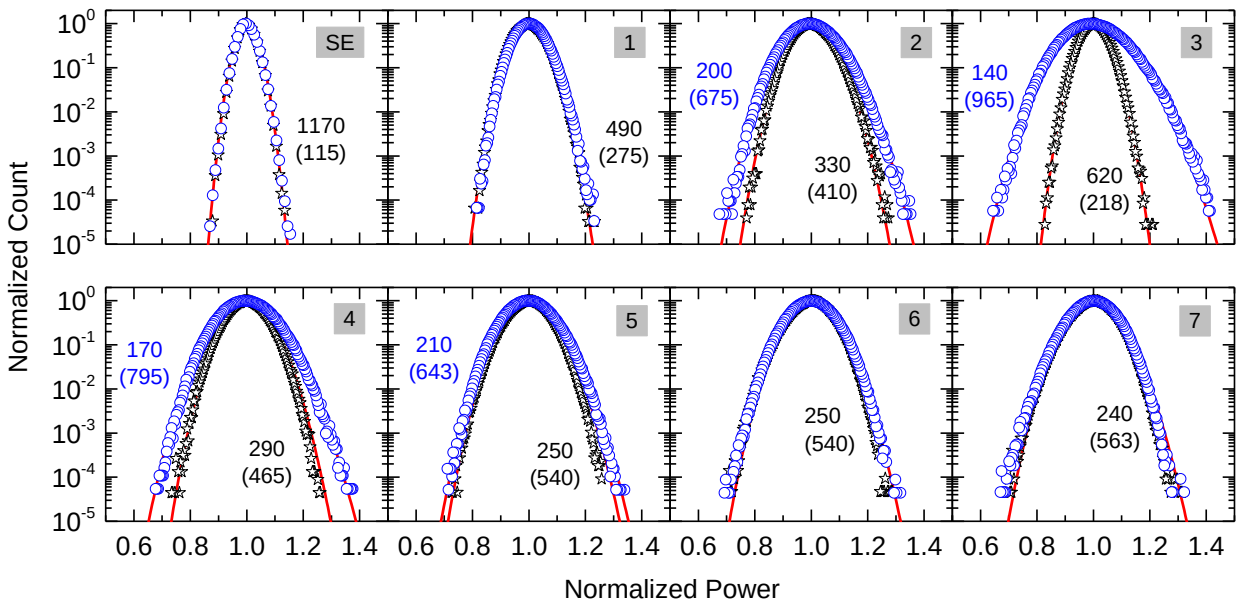

Figure 39. Normalized photon distributions obtained for ASE when the AOM1 is closed (the top-left window, marked as SE) and for different sub-pulses, observed within AQS pulse for ring EDFL (the rest of the windows). Each window shows two kinds of distributions: directly at the laser output (black stars) and after being propagated through 100-m SMF-28 fiber (blue circles). The red curves are fits by Poissonian distributions; the photon numbers used in simulations are given near each curve as well the mode number is in brackets.

The minimum $\bar{n}$ is obtained for the most powerful (main) sub-pulse and relates to the broadest ASE bandwidth. In contrast to the EDFL with a F-P cavity, no "cuts" in the tail of the photon noise distributions were obtained at high powers of noise peaks since the sub-pulse wave is composed of many modes (hundreds) that oscillate around the mean value of optical power, thus all of them have almost the same probability to be depleted as it is seen in most powerful sub-pulses shown in Figure 40.

Note that the real widths of the photon distributions described by Poissonian statistics are smaller because, for each sub-pulse in the train, new longer wavelengths was created due to Raman scattering effect. In this case, the effective optical spectrum width of the AQS pulses reaches the value of the order of tens nanometers, which is less by more than 2 orders than that in the F-P laser.

It is important to stress that generation of the new wavelengths in ring laser configuration arise partly from MI and partly from Raman scattering in contrast to dominating of MI in F-P laser. This statement will be discussed in the following chapter.

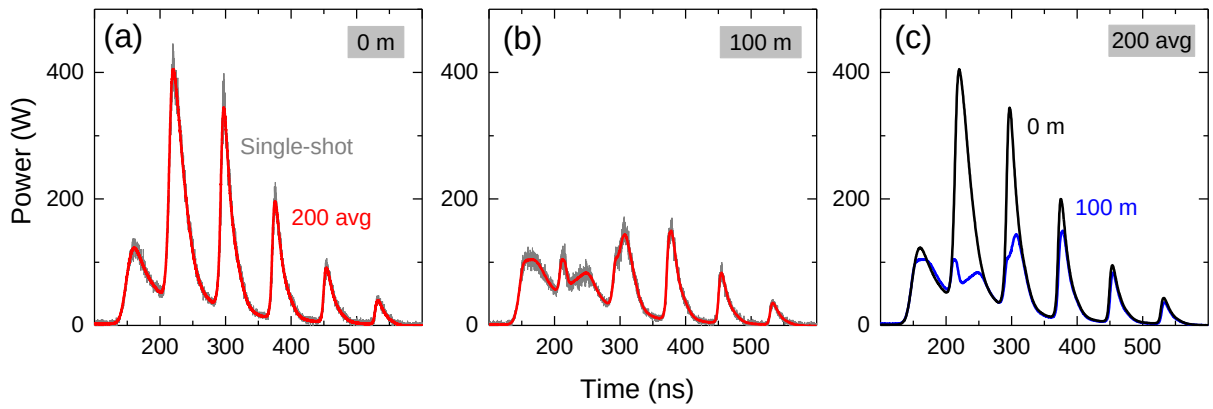

Figure 40. Oscilloscope traces of averaged (red curve) and single-shot (grey curve) AQS pulses from ring FLs. Traces in (a) and (b) correspond to the measurements done directly on the lasers' output and after passing 100 m of SMF-28, respectively. (c) Shapes of averaged AQS pulses measured on FL output (black line) and after 100 m of SMF-28 fiber (blue line).

In summary, in this chapter we report the photon statistics of AQS EDFLs, comparing its features for the lasers with F-P and ring cavities. First, we demonstrate that, in general, AQS pulses coming from the F-P EDFL are noisier than those from the ring FL. Accordingly, the photon distributions in the F-P FL are broader, by approximately 2 orders, than in the ring one. Second, by means of modeling the distribution of the noise statistics of spectrally filtered ASE that forms all sub-pulses in the case of the F-P EDFL, we show that the noise distributions, for either sub-pulse, are well fitted by very broad $M-$ fold degenerate Bose-Einstein distributions. Also, modeling the noise statistics of nonfiltered ASE of which consist all sub-pulses in the case of the ring laser, we reveal that their noise distributions are fitted by Poissonian distributions. This technique allows us to study correlations between spectral width and photon distribution for each sub-pulse.

Finally, understanding the processes behind AQS pulsing in EDFLs provide guidance for making a proper choice of an AQSL scheme, permitting one to predict, or control, the noise statistics of AQS pulses, which may be valuable for such applications as supercontinuum generations.

Chapter 5 Nonlinear Processes Arising in Actively Q-switched Fiber Lasers

In this chapter, the spectral dynamics, arising for each sub-pulse of which the whole AQS pulse is composed, will be discussed and compared for AQS EDFLs based on the F-P and the ring cavities. As it was mentioned above, the lasers under study are frequency-shifted multi-pass amplifiers of ASE filtered by FBGs when the laser is based on F-P cavity or non-filtered ASE when ring cavity is used. Since the mean peak power of AQS pulses from these lasers is rather high, up to 500 W, a few nonlinear optical processes, such as modulation instability (MI), self-phase modulation (SPM), and Raman scattering (RS) occur. Note that stimulated Brillouin scattering (SBS) is not observed in these two lasers since the laser linewidth is broad enough, of the order of 10 GHz and higher for the F-P AQSL, and of the order of THz for the ring AQSL. Nonlinear effects mentioned above can be detrimental or useful, depending on the purpose of application of the AQSL.

It is known that in Q-switched fiber lasers, SPM and MI provide symmetric spectral broadening and RS is responsible for asymmetric spectral broadening [52]. In fact, these effects may coexist in Q-switched FLs and interact with each other both inside and outside the FL cavity. In other words, depending on the AQS pulse width, peak power and also on the type and length of fiber used in FL cavity and on the laser output, dispersive or nonlinear effects may dominate in the pulse propagation.

For a discussion of the influence of spectral broadening effects, it is useful to introduce two characteristic lengths, known as the *dispersion length* L_{D} and the *nonlinear length* L_{NL}. The dispersion length defines a length over which dispersion of the fiber is important for pulse evolution. It is approximately equal to the propagation length required for a transform-limited Gaussian pulse to be double in duration due to fiber dispersion. The value of the dispersion length is found as [52]

$$L_{\mathrm{D}} = \frac{T_0^2}{|\beta_2|}, \tag{15}$$

where T_0 is the half-width (at 1/*e*-peak power) before interacting with a fiber and β_2 is the group velocity dispersion (GVD) parameter. In practice, it is customary to use the width measured at 3-dB instead of T_0. For a Gaussian pulse, such time widths are related as [52]

$$T_0 = \frac{T_{3\,\mathrm{dB}}}{2\sqrt{\ln 2}} \approx 0.6 T_{3\,\mathrm{dB}}. \tag{16}$$

The fiber dispersion highly affects short pulses (below picoseconds) rather than the long (nanosecond) pulses (the case of ring AQS pulses). However, it is worth noting that F-P AQS pulses are composed of many fluctuations instead of a smooth envelope; thus, we can estimate the fluctuations' width assuming them as short transform-limited random Gaussian pulses. One can also estimate the minimum value of noise pulse duration, $T_{3\,\mathrm{dB}}$, from the bandwidth of F-P AQSL, which equals to approximately 50 pm ($\Delta\nu_{3\,\mathrm{dB}} = 6.3$ GHz) on the laser output in the absence of SPM effect (see the theoretical red dashed curve in Figure 29 for the 4th sub-pulse). In that case, the minimum (noise) pulse duration is given by [53]

$$T_{3\,\mathrm{dB}} \approx \frac{0.441}{\Delta\nu_{3\,\mathrm{dB}}} = 70\ \mathrm{ps}. \tag{17}$$

Substituting eq. (16) and eq. (17) in eq. (15) for known SMF-28 fiber (at 1.55 μm the value of GVD is $\beta_2 \approx\sim -22$ ps²/km [52]), for noise pulse fluctuations we have a fiber dispersion length of $L_D \approx 80\,200$ m. Such length is tremendously long in comparison with 100 m used in the experiment. However, dispersion length is not the only one that characterizes the propagation of the pulses as will be shown below.

The nonlinear length is the pulse propagation length after which nonlinear effects become significant. This length is found as

$$L_{\mathrm{NL}} = \frac{1}{\gamma P_p}, \tag{18}$$

here P_p is the pulse peak power, and γ is the nonlinear parameter that depends on the effective mode area and the composition of the material used for optical waveguide. The nonlinear parameter is given by [52]

$$\gamma = \frac{\omega_0 n_2}{c A_{\text{eff}}}, \tag{19}$$

where ω_0 is the central laser frequency, $n_2 \approx 2.6 \times 10^{-20}$ m^2/W is the nonlinear refractive index for silica glass fiber, and $A_{\text{eff}} = \pi w^2 / 2$, is the effective area of the Gaussian propagation mode, where $2w$ is the mode field diameter of the fiber at the laser wavelength. The nonlinear parameter of SMF-28 fiber is $\gamma \approx 1.1$ (W km)$^{-1}$ [52], and the peak power of the main sub-pulse (the 4th in Figure 35 (a)) is 500 W, thus, one obtains using eq. (18) the nonlinear length: $L_{NL} \approx 1.8$ m. Since for the main sub-pulse the following condition is satisfied: $L_{NL} < L \ll L_D$ (where *L* equals to a few meters that is the FL cavity length plus a short fiber piece on the output of the cavity), it propagates along the fiber in the strong nonlinear regime, in which the pulse propagation is governed by SPM resulting in changes in the pulse spectrum as it is seen from Figure 29 and also will be discussed below.

When L_D and L_{NL} are of the same order (*e.g.*, T_0 is small enough) and the fiber length L is longer or comparable to both of these lengths, dispersion and nonlinearity act together as the pulse propagates along the fiber. It is worth mentioning that in the anomalous-dispersion regime ($\beta_2 < 0$) long pulses present MI, generating soliton trains that undergo in a soliton dynamic phase, which characterized by a broadband spectrum [51], [54], [55].

Below the nonlinear effects in the aforementioned Q-switched EDFLs will be analyzed experimentally, with focusing on the spectral and on the temporal dynamics involved in the AQS laser pulsing. Spectral broadening and Raman scattering effects will be also discussed.

5.1 Spectral line broadening effect in Q-switched fiber lasers

Actively Q-switched fiber laser generates relatively long (ns range) and powerful pulses (tenths watts to a few kilowatts) that increase the modal refractive index as a function of light intensity in the fiber core, generally radial-dependent (usually is omitted). This nonlinear effect is called the Kerr ef-

fect. This effect induces the so-called self-phase modulation resulting in the generation of new frequency components around the spectrum line of the "pump" pulse.

In the presence of an optical field with a time-varying optical intensity (i.e. $I = I(t)$), the nonlinear contribution to the local refractive index across an optical pulse will cause a time-dependent nonlinear phase delay, $\varphi_{\mathrm{NL}}(t) = 2\pi n_2 z I(t)/\lambda$, where n_2 is the above mentioned nonlinear refractive index, and z is a coordinate along the fiber. This effect will, in turn, leads to a shift in the instantaneous optical frequency across the pulse according to the relationship

$$\Delta\omega = -\frac{\partial \varphi_{\mathrm{NL}}(t)}{\partial t}. \tag{20}$$

Assuming $z > 0$, the frequency shift is negative (downshift) for the leading edge of the pulse, and positive (up-shift) for the trailing edge, thus, the new optical frequency components arise. The values of widths of all sub-pulses' spectra measured on the fiber laser output marked as "0 m" (after 3 m passive fiber) are shown in Figure 41 by the black curve together with the theoretical result obtained using eq. (14) and depicted by the blue curve.

When the output laser pulses are coupled into a very long piece (100 m) of SMF-28 fiber (marked as "100 m"), the spectral width of powerful sub-pulses increases stronger, as it is seen from the red curve in Figure 41. The spectral widths of the sub-pulses 3rd and 5th increase by three times and of the 4th (main) sub-pulse by 20%, all with respect to that obtained on the laser output (see the red curve in Figure 41), while it remains unchanged for the low-power sub-pulses, i.e., the sub-pulses 1st, 2nd, 6th and 7th.

It is worth to mention that analytical expression for eq. (20) does not exist for thermal light in anomalous dispersion regime to the best of our knowledge. However a phenomenological model where the fluctuation has been modeled by a sinusoidal law with an offset has been recently made in normal dispersion regime for silica fibers [56].

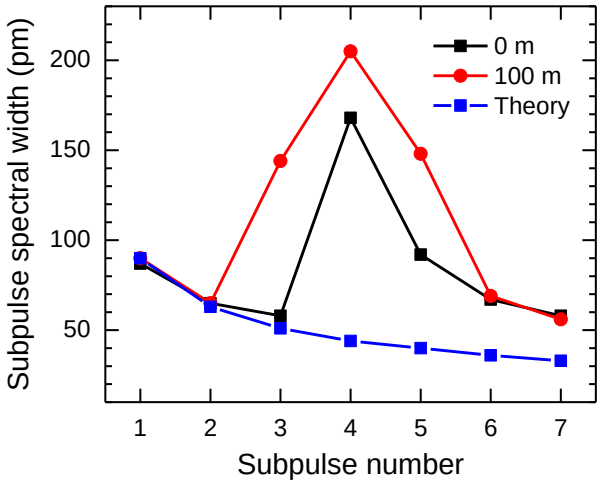

Figure 41. Widths of optical spectra of different sub-pulses measured at 3-dB level. The black curve corresponds to widths measured on the laser output (3-m long passive fiber), the red curve shows the widths measured after 100-m of SMF-28 fiber. The blue curve demonstrates values obtained using eq. (14) in which nonlinear effects are omitted.

The spectral broadening observed due to nonlinear interaction of pulses from the ring AQSL with optical fiber is more complicated than for the pulses from the F-P AQSL, since the SPM is not the only nonlinear phenomenon involved. Figure 42 shows the sub-pulses' spectra before (solid black line) and after (solid red line) propagating along 100 m-piece of SMF-28 fiber.

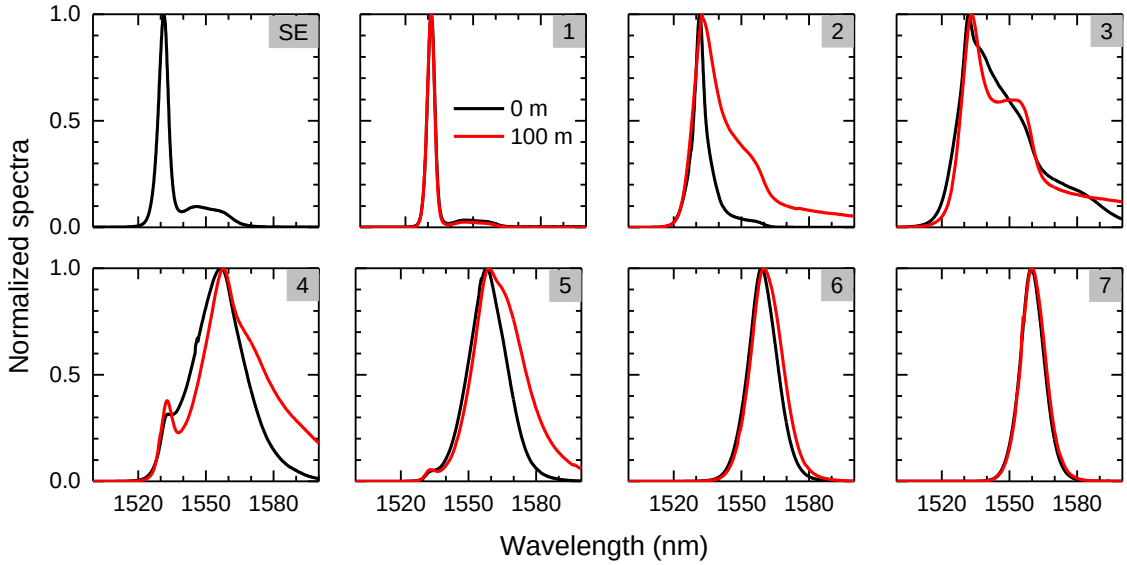

Figure 42. Spectra of the amplified spontaneous emission (marked as SE) and of the sub-pulses composing AQS pulse measured at the F-P AQS EDFL output (black line) and after 100-m long communication fiber (solid red line). It is seen that a spectral broadening arises for the sub-pulses with numbers from 2 to 6 after their propagating through the long fiber.

It is worth noting that the SPM phenomenon does not affect the amplitude neither the shape of AQS pulses for theirs time widths and length scales discussed in the thesis; instead, SPM increases the

optical bandwidth and hence changes widths of histograms of photon counts for both Poisson and Bose-Einstein statistics. Finally, the shapes of the histograms of photon counts (photon noise) are not affected by SPM, but MI and Raman scattering could indeed deplete the most intense sub-pulse and therefore deform the histograms shapes as it will be discussed below.

5.2 Modulation Instability in Q-switched fiber lasers

In this section, we expose briefly the MI effect that leads to extra-broadening of AQS pulse. The MI effect is characterized by two spectral sidebands around the pump wavelength. However, even if the amplitude of the input pulse is stable, the output (not averaged) spectrum demonstrates strong variations when measured for different pulses [50]. Moreover, the averaged spectrum yields a characteristic triangular shape when plotted in semi-logarithmic scale [31]. The analysis of MI effect can only be treated numerically by solving the nonlinear Schrödinger equation (NLSE), which provides an exact solution to the problem [31], [50]–[52], [55]. Numerical simulations using NLSE is out of the scope of this thesis. On the other hand, to qualitatively describe the phenomena involved in spectral broadening of the AQS pulses the known solutions of NLSE will be used.

It is shown that the spectrally-dependent gain of MI depends on the dispersion characteristics of the fiber as well as on the input power. For the highest spectral sidebands, the central frequency spacing is given by [52]

$$\frac{\Omega_{\max}}{2\pi} = \pm\frac{1}{\pi}\sqrt{\frac{\gamma P_p}{2|\beta_2|}}, \tag{21}$$

where γ is the nonlinear coefficient mentioned above. For 80 W of peak power, we found from eq. (21) that the MI sidebands match with the experimental frequency value of ±0.45 THz.

The sidebands' growth is initiated by intensity fluctuations within the picosecond to nanoseconds range of pump pulses. At the beginning of the process, sidebands' spectral amplitudes grow exponentially with the propagation distance, and then, at higher sidebands' intensities, the growth continues as long as the fraction of the power in these sidebands remains a small fraction of the total power. This is the so-called linear regime that is characterized by a "triangular" shape of the wings in the spectral domain when presented in the semi-logarithmic scale (see spectra of the 3rd and 5th sub-pulses of ASE pulse from F-P AQS EDFL shown in Figure 43). In the time domain the pulses are

characterized by localized breathers [31], [50], [51], [55]. When the fraction of the power in the side-bands remains an essential fraction of the total power, the MI process enters the so-called nonlinear regime. In this regime, the pump pulses deplete that results in the complex evolution of the optical field, where early soliton formation and Raman scattering begin to play an important role, adding more spectral components to the Stokes region, as it is demonstrated by the spectrum of the 4th sub-pulse in Figure 43.

The break-up of a long pulse has later been related to the Akhmediev breather theory [54], [57]. Akhmediev breathers are exact analytical solutions to the NLSE that describes the evolution of a pump wave with a small periodical perturbation imposed on constant background intensity, resulting in the narrowing and broadening (breathing effect) of a train of ultrashort pulses. It was suggested in [31] that the onset of long-pulse SC generation from spontaneous MI can be interpreted as the generation of a large number of Akhmediev breathers that then transform into solitons.

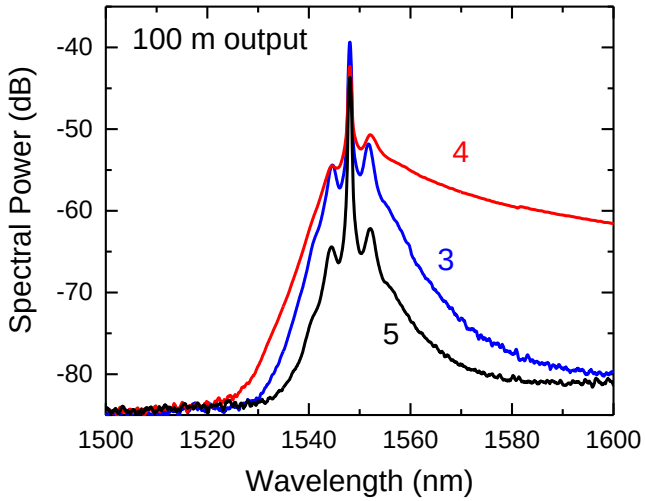

Figure 43. Spectra of the 3th, 4th, and 5th sub-pulses of ASE pulse from F-P AQS EDFL measured after propagation along 100-m communication fiber. AOM2 with tunable gate delay was used for separating the spectra of either sub-pulse under study.

We will focus here on the characteristics of the MI spectrum affecting the photon count distribution of the 3rd to 5th sub-pulses collected at the output of the 100-m long SMF-28 fiber (see Figure 43). Note that, since the optical spectra are obtained using available standard OSAs, always with a slow sweep speed, the sidebands' spectra are well averaged, so the information about fast processes related to the noise nature of the MI bands is lost. However, the depletion caused by MI is capable of "cut" the right-hand tail of the photon count distributions as can be seen for sub-pulses 3rd, and 5th

(blue circles) in Figure 37, and in the case of the 4th sub-pulse, dramatically increases (by an order) the mode number correspondent to the photon statistics of the pulses registered after propagating along the 100-m communication fiber.

The spectral broadening observed in sub-pulses composing ASE pulse from the ring AQS EDFL is always asymmetrical (see Figure 42), and is described by a mixture of the MI and Raman effect [58], [59]. This mixture arises when broadband (tens nanometers) light pulses interacts with optical fiber, which results in generating new spectral components at longer wavelengths. Generation of new wavelengths affects the Poisson photon distribution, characterizing broad-band light sources, by decreasing the mean photon number per mode due to increase some modes, as can be seen in Figure 39. Significantly stronger depletion in power is observed for the 3rd and the 4th sub-pulses for which soliton dynamics generates long wavelengths; also, at the same time and independently, a low stimulated Raman peak around 1670nm arises (see inset to Figure 31 (b)). In silica-based fibers, the peak of the Raman gain is downshifted by $f_R = 13.2$ THz; thus, for the peak of the sub-pulse 4th at 1560 nm the corresponding shift of the peak is about 115 nm. Thus, the first Raman peak arises at 1675 nm, with a bandwidth of about 50 nm [60].

In actively Q-switched fiber lasers with a cavity length of about ten meters (the case of our experimental arrangement), chromatic dispersion does not take effect on a pulse envelope, but the Raman Stokes signal arises and co-propagate with Q-switched “pump” pulses [61]. Such kind of fiber laser operation significantly differs from these operating in continuous wave regime, in which both the co- and the counter-propagating Stokes waves are significant in the presence of SRS [62]. The detrimental SRS phenomenon consists of two effects: in the spectral domain, the undesired Raman components appear; in the temporal domain, the signal pulse may undergo some distortion, and the total pulse energy suffers from a certain loss. SRS in pulsed fiber lasers and amplifiers operated with nanosecond pulses at repetition rate of tens kHz [63]–[67] is distinct from that with picosecond or femtosecond pulses with repetition rates typically of tens MHz [68]–[70]. In the former, the evolution of ASE and population inversion in the interval between two consecutive pulses and during them plays an important role in maintaining the pulse with certain energy and waveform as compared with the effect of GVD, SPM, gain bandwidth and the walk-off effect that govern pulse propagation in the latter [52]. However, a mixture of nonlinear MI regime and SRS is currently unclear.

The next part of the experimental study relates the impact of intra-pulse Raman scattering of femtosecond noise pulses in spectral broadening of nanosecond AQS pulses.

5.3 Supercontinuum Generation by AQS Pulses in a Long Communication Fiber

It is seen from the preceding discussion that the noise nature of the AQS pulses plays a crucial role in nonlinear processes accompanying spectral broadening and supercontinuum generation (SCG) since they are seeded by the MI effect. This effect causes the breakup of the transient part of pump pulse to a set of short pulses with different widths and powers; the subsequent Raman effect-induced frequency shift results in the spectral broadening of the output signal. At the same time, a part of the Q-switch pulse may be sufficiently smooth to be free of these short pulses and thus promotes conventional Stokes generation (see the line marked as 4 in the inset to Figure 31). This effect also has been observed when nanosecond pulses from a diode laser propagate along the optical fiber [71].

The MI-generated solitons consist of a large number (several hundred or more ultrashort pulses) with essentially random parameters [72, Ch. 10], these will be redshifted at different velocities, which inevitably leads to temporal collisions. In fact, it turns out that inelastic soliton collisions are a key effect in the formation of the long-wavelength SC edge [73]–[75]. During such collisions, inter-pulse collision transfers energy between the solitons; this energy transfer depends strongly on the relative phase and amplitude, but generally there is a preferential transfer of energy from the smaller to the larger soliton, where the shortest pulses exhibit the largest shift [73]–[75]. The most powerful soliton broadens and slows down before reaching the infrared silica loss edge, which effectively prevents soliton propagation beyond ~ 2.2 μm.

In summary, we demonstrated the potential of using nanosecond-range AQS pulses (from both F-P and ring fiber lasers) for generating supercontinuum in a 100-m piece of SMF-28 fiber. Particularly, we show that SC is effectively generated by the highest in magnitude sub-pulses in the AQS train, consuming the most of its energy, while the remaining sub-pulses are not effective for SC generation.

Chapter 6 Conclusions

6.1 Spectral Dynamics

In this thesis, the dynamics of optical spectrum of AQS EDFL was reported. The spectra were measured separately for each sub-pulse of train composing a “whole” AQS pulse, emphasizing its details inherent to the two conventional EDFL schemes based on F-P and ring cavities.

It was shown that optical spectrum of the laser assembled in the ring configuration moves towards longer wavelengths stepwise in each sub-pulse sequencing in the train, with the total shift ~30 nm, the effect has been connected with a gradual depopulation of the laser level of erbium ions by each consequent sub-pulse. On the other hand, the laser arranged in the F-P configuration does not demonstrate such spectral shifting as its line was fixed at the wavelength selected within the EDF gain spectrum by FBG couplers.

In both cavity configurations, the optical spectrum width strongly depended on the sub-pulses number. The width of optical spectra of sub-pulses measured in the F-P laser scheme varies from ~55 to ~200 pm while in the ring one it changed from ~4 to ~30 nm, with the spectrum of the “main” (most powerful) sub-pulse being much wider than those of the rest (less powerful) ones. The effect of EDFL spectrum broadening in the first case appeared due to such nonlinear effects as self-phase modulation and modulation instability, whereas in the second case it adheres to the EDF gain (inversion) spectral dynamics over the sub-pulses’ train, the effect being most notable for the “main” sub-pulse, during which a very fast depopulation of the laser level takes place.

We also demonstrated the potential of using nanosecond-range AQS pulses (from both lasers under study) for generating supercontinuum in a 100-m piece of SMF-28 fiber, paying attention to its effect on noise photon statistics. Particularly, we show that SC is effectively generated by the highest in magnitude sub-pulse in the AQS train, consuming the most of its energy, while the remaining sub-pulses are not effective in SC generation. The present study is important for understanding the pro-

cesses behind AQS pulsing in EDFLs. For instance, it guides making a proper choice of an AQS EDFL scheme, permitting one to predict, or control, the noise statistics of AQS pulses, which may be valuable for such applications as SC generation.

6.2 Temporal Dynamics

In this thesis, we report the photon noise statistics of AQS EDFLs, comparing its features for the lasers with F-P and ring cavities; we address the phenomenon both experimentally and theoretically. For both configurations, the AQS EDFL is considered as a multi-pass amplifier, implying, however, that for the laser with the F-P cavity ASE is reflected several times by narrowband FBGs while for the ring one it makes a few unidirectional passes along the loop-free from spectrally selective components.

First, we demonstrate that, in general, AQS pulses from the F-P EDFL are noisier than those leaving the ring FL. Accordingly, the probability distribution of pulsing in the F-P FL is broader, by approximately two orders, than in the ring one. Second, applying an original technique to separate the noise photon statistics for sub-pulses of which AQS pulses consist, we analyze fine details of noise properties of all sub-pulses, for both laser configurations.

Then, by means of modeling the noise statistics of spectrally filtered ASE that forms all sub-pulses in the case of the F-P EDFL, we show that the noise histograms, for either sub-pulse, are well fitted by very broad M-fold degenerate Bose-Einstein distributions, with the peaks of noise exceeding the mean power by about an order of magnitude.

Modeling the noise statistics of nonfiltered ASE of which consist all sub-pulses in the case of the ring laser, we reveal that their noise histograms are fitted by narrow Poissonian distributions, with noise fluctuations not exceeding $\sim 10\%$ of the mean power, in our experimental conditions.

For both laser geometries, the noise distributions of the main (most powerful) sub-pulses are always much broader as compared with the ones of other, less powerful, sub-pulses.

We are convinced that the present study is important for understanding the processes behind AQS pulsing in EDFLs and also can be extended to other amplified-spontaneous-emission-based AQS.

6.3 Future development

The development and results of the present dissertation work raise a set of new ideas and proposals which could be carried out in the nearest future.

First, it was demonstrated that AQS pulses from EDFL might be successfully used as a pump for supercontinuum generation (SCG) in nonlinear fibers. It was shown that under the action of nonlinear effects involved to SCG the pulses are cut at the level of approximately 100 W, their shape measured after the nonlinear fiber is distorted demonstrating a hole at the pulse center instead of a peak. However these measurements were fulfilled without spectral selection of the laser wavelength, so a part of supercontinuum (SC) was also captured by the photodetector. This effect also affected results of photon statistics. Thus, in the future, we plan to study the effect of SCG on AQS pulses by measuring the shape of the pulses and their photon statistics after narrow-band optical filtering of the laser wavelength. We also plan to study statistics of SC for different wavelengths after narrow-band optical filtering and compare them with that of the AQS pulses.

It was also demonstrated that using so-called smart Q-switching [76] one can obtain sole AQS pulses (without sub-pulses) with peak power up to 1.5 kW and probably higher. We plan to adopt this technique for SCG [77] and for measuring photon statistics as it was noted above.

In addition, we plan to model AQS fiber laser including a smart one using a model of two contra-propagating waves (distributed model) with accounting radial distribution of the pump and the laser waves. Preliminary we have obtained that only when the radial distributions of the waves are considered to the model, the law of energy conservation is satisfied [78]. This modeling permits us to optimize the laser parameters for reaching the maximum peak power for further usage, for example, SCG, and other tasks.

Finally, we plan to model SCG using the nonlinear Schrödinger equation applied to the case when nanosecond pulses with photon noise characterized by Bose-Einstein distribution are used for pumping nonlinear fiber. This study will help us to understand deeper the physics behind this process.

References

[1] M. J. F. Digonnet, *Rare-Earth-Doped Fiber Lasers and Amplifiers, Revised and Expanded*. Taylor & Francis, 2001.

[2] L. Dong and B. Samson, *Fiber Lasers: Basics, Technology, and Applications*. CRC Press, 2016.

[3] A. Piper, A. Malinowski, K. Furusawa, and D. J. Richardson, "High-power, high-brightness, mJ Q-switched ytterbium-doped fibre laser," *Electron. Lett.*, vol. 40, no. 15, p. 928, 2004.

[4] A. E. Siegman, *Lasers*. Oxford: Oxford University, 1986.

[5] D. J. Richardson, J. Nilsson, and W. a. Clarkson, "High power fiber lasers: current status and future perspectives [Invited]," *J. Opt. Soc. Am. B*, vol. 27, no. 11, p. B63, Nov. 2010.

[6] P. Myslinski, J. Chrostowski, J. A. Koningstein, and J. R. Simpson, "High power Q-switched erbium doped fiber laser," *IEEE J. Quantum Electron.*, vol. 28, no. 1, pp. 371–377, 1992.

[7] Y. Wang and C.-Q. Xu, "Understanding multipeak phenomena in actively Q-switched fiber lasers," *Opt. Lett.*, vol. 29, no. 10, p. 1060, May 2004.

[8] S. A. Kolpakov *et al.*, "Distributed Model for Actively Q-Switched Erbium-Doped Fiber Lasers," *IEEE J. Quantum Electron.*, vol. 47, no. 7, pp. 928–934, Jul. 2011.

[9] G. P. Lees and T. P. Newson, "Diode pumped high power simultaneously q-switch and self mode-locked erbium doped fibre laser," *Electron. Lett.*, vol. 32, no. 4, pp. 332–333, 1996.

[10] R. Zhou, W. Shi, E. Petersen, A. Chavez-Pirson, M. Stephen, and N. Peyghambarian, "Transform-Limited, Injection Seeded, Q-Switched, Ring Cavity Fiber Laser," *J. Light. Technol.*, vol. 30, no. 16, pp. 2589–2595, Aug. 2012.

[11] Y. O. Barmenkov, A. V. Kirryanov, J. L. Cruz, and M. V. Andres, "Pulsed Regimes of Erbium-Doped Fiber Laser Q-Switched Using Acousto-Optical Modulator," *IEEE J. Sel. Top. Quantum Electron.*, vol. 20, no. 5, pp. 337–344, Sep. 2014.

[12] X. Lü, Q. Han, T. Liu, Y. Chen, and K. Ren, "Actively Q-switched erbium-doped fiber ring laser with a nanosecond ceramic optical switch," *Laser Phys.*, vol. 24, no. 11, p. 115102, Nov. 2014.

[13] Y. Wang and C. Q. Xu, "Actively Q-switched fiber lasers: Switching dynamics and nonlinear

processes," *Prog. Quantum Electron.*, vol. 31, no. 3–5, pp. 131–216, 2007.

[14] J. Swiderski, A. Zajac, P. Konieczny, and M. Skorczakowski, "Numerical model of a Q-switched double-clad fiber laser.," *Opt. Express*, vol. 12, no. 15, pp. 3554–3559, 2004.

[15] J. K. Jabczynski *et al.*, "Actively Q-switched Thulium Lasers," in *Advances in Solid State Lasers Development and Applications*, M. Grishin, Ed. Rijeka: InTech, 2010.

[16] J. Geng, Q. Wang, Z. Jiang, T. Luo, S. Jiang, and G. Czarnecki, "Kilowatt-peak-power, single-frequency, pulsed fiber laser near 2 µm," *Opt. Lett.*, vol. 36, no. 12, p. 2293, Jun. 2011.

[17] Y. O. Barmenkov, S. A. Kolpakov, A. V. Kir'Yanov, L. Escalante-Zarate, J. L. Cruz, and M. V. Andres, "Influence of cavity loss upon performance of Q-switched erbium-doped fiber laser," *IEEE Photonics Technol. Lett.*, vol. 25, no. 10, pp. 977–980, 2013.

[18] S. A. Kolpakov, S. Sergeyev, Chengbo Mou, N. T. Gordon, and Kaiming Zhou, "Optimization of Erbium-Doped Actively Q-Switched Fiber Laser Implemented in Symmetric Configuration," *IEEE J. Sel. Top. Quantum Electron.*, vol. 20, no. 5, pp. 329–336, Sep. 2014.

[19] E. Desurvire, *Erbium-doped fiber amplifiers: principles and applications*. Wiley-Interscience, 2002.

[20] P. Adel, *Pulsed Fiber Lasers*. Cuvillier, 2004.

[21] S. Tammela, M. Söderlund, J. Koponen, V. Philippov, and P. Stenius, "The potential of direct nanoparticle deposition for the next generation of optical fibers," *Proc. SPIE*, vol. 6116, 2006.

[22] J. W. Fleming, S. Kakar, R. M. Lum, and E. M. Monberg, "Process for fabricating optical fiber involving overcladding during sintering," US Patent # 6446468, 2002.

[23] a. D. Guzman-Chavez, Y. O. Barmenkov, and A. V. Kir'yanov, "Spectral dependence of the excited-state absorption of erbium in silica fiber within the 1.48–1.59µm range," *Appl. Phys. Lett.*, vol. 92, no. 19, p. 191111, May 2008.

[24] Yong Wang and Chang-Qing Xu, "Switching-induced perturbation and influence on actively Q-switched fiber lasers," *IEEE J. Quantum Electron.*, vol. 40, no. 11, pp. 1583–1596, Nov. 2004.

[25] C. C. Ranaud *et al.*, "Characteristics of Q-switched cladding-pumped ytterbium-doped fiber lasers with different high-energy fiber designs," *IEEE J. Quantum Electron.*, vol. 37, no. 2, pp. 199–206, 2001.

[26] D. J. Ripin and L. Goldberg, "High efficiency side-coupling of light into optical fibres using imbedded v-grooves," *Electron. Lett.*, vol. 31, no. 25, pp. 2204–2205, Dec. 1995.

[27] T. Weber, W. L?thy, H. P. Weber, V. Neuman, H. Berthou, and G. Kotrotsios, "A longitudinal and side-pumped single transverse mode double-clad fiber laser with a special silicone coating," *Opt. Commun.*, vol. 115, no. 1–2, pp. 99–104, Mar. 1995.

[28] J.-L. Archambault and S. G. Grubb, "Fiber gratings in lasers and amplifiers," *J. Light. Technol.*, vol. 15, no. 8, pp. 1378–1390, 1997.

[29] M. Sejka, C. V. Poulsen, J. H. Povlsen, Y. Shi, and O. Poulsen, “High Repetition Rate Q-Switched Ring Laser in Er3+-Doped Fiber,” *Opt. Fiber Technol.*, vol. 1, no. 2, pp. 167–170, Mar. 1995.

[30] S. A. Kolpakov, Y. O. Barmenkov, A. Kir’yanov, L. Escalante-Zarate, J. L. Cruz, and M. V. Andres, “Smooth Pulse Generation by a Q-Switched Erbium-Doped Fiber Laser,” *IEEE Photonics Technol. Lett.*, vol. 25, no. 5, pp. 480–483, Mar. 2013.

[31] J. M. Dudley, G. Genty, F. Dias, B. Kibler, and N. Akhmediev, “Modulation instability, Akhmediev Breathers and continuous wave supercontinuum generation,” *Opt. Express*, vol. 17, no. 24, p. 21497, Nov. 2009.

[32] S. Adachi and Y. Koyamada, “Analysis and Design of Q -Switched Erbium-Doped Fiber Lasers and Their Application to OTDR,” *J. Light. Technol.*, vol. 20, no. 8, pp. 1506–1511, 2002.

[33] P. Roy and D. Pagnoux, “Analysis and Optimization of a Q-Switched Erbium Doped Fiber Laser Working with a Short Rise Time Modulator,” *Opt. Fiber Technol.*, vol. 2, no. 3, pp. 235–240, 1996.

[34] H. S. Nalwa, *Photodetectors and Fiber Optics*. Academic Press, 2001.

[35] B. E. A. Saleh, *Photoelectron statistics, with applications to spectroscopy and optical communication*, 1st ed. Springer-Verlag, 1978.

[36] J. W. Goodman, *Statistical Optics*. Wiley.

[37] A. Mecozzi, “Quantum and semiclassical theory of noise in optical transmission lines employing in-line erbium amplifiers,” *J. Opt. Soc. Am. B-Optical Phys.*, vol. 17, no. 4, pp. 607–617, 2000.

[38] T. Li and M. C. Teich, “Photon point process for traveling-wave laser amplifiers,” *IEEE J. Quantum Electron.*, vol. 29, no. 9, pp. 2568–2578, 1993.

[39] S. M. Pietralunga, P. Martelli, and M. Martinelli, “Photon statistics of amplified spontaneous emission in a dense wavelength-division multiplexing regime.,” *Opt. Lett.*, vol. 28, no. 3, pp. 152–154, 2003.

[40] A. R. Karthikeyan and H. S. Ramachandran, “Convergence of quantum and semiclassical models of erbium-doped fiber amplifiers,” *J. Opt. Soc. Am. B Opt. Phys.*, vol. 28, no. 3, pp. 533–542, 2011.

[41] L. Mandel and E. Wolf, *Optical Coherence and Quantum Optics*. New York: Cambridge University Press, 1995.

[42] Y. O. Barmenkov, A. V. Kir’yanov, and M. V. Andres, “Nonlinear dynamics of Ytterbium-doped fiber laser Q-switched using acousto-optical modulator,” *Eur. Phys. J. Spec. Top.*, vol. 223, no. 13, pp. 2775–2788, Dec. 2014.

[43] D. N. Schimpf, C. Ruchert, D. Nodop, J. Limpert, A. Tünnermann, and F. Salin, “Compensation of pulse-distortion in saturated laser amplifiers,” *Opt. Express*, vol. 16, no. 22, pp. 17637–17646, Oct. 2008.

[44] Y. Xiao, F. Brunet, M. Kanskar, M. Faucher, A. Wetter, and N. Holehouse, “1-kilowatt CW all-fiber laser oscillator pumped with wavelength-beam-combined diode stacks,” *Opt. Express*, vol. 20, no. 3, pp. 3296–3301, Jan. 2012.

[45] K. Hejaz *et al.*, “Decreasing effective reflectivity of the output coupler in the power scaling of fiber lasers,” *Laser Phys. Lett.*, vol. 13, no. 3, p. 35107, Mar. 2016.

[46] R. H. Stolen, C. Lee, and R. K. Jain, “Development of the stimulated Raman spectrum in single-mode silica fibers,” *J. Opt. Soc. Am. B*, vol. 1, no. 4, pp. 652–657, Aug. 1984.

[47] Yong Wang, “Dynamics of stimulated Raman scattering in double-clad fiber pulse amplifiers,” *IEEE J. Quantum Electron.*, vol. 41, no. 6, pp. 779–788, Jun. 2005.

[48] F. J. McAleavey and B. D. MacCraith, “Diode-pumped thulium-doped zirconium fluoride fibre as fluorescent source for water sensing ,” *Electron. Lett.*, vol. 31, no. 16, pp. 1379–1380, 1995.

[49] A. V Kir’yanov, Y. O. Barmenkov, and M. V Andres, “An experimental analysis of self- Q -switching via stimulated Brillouin scattering in an ytterbium doped fiber laser,” *Laser Phys. Lett.*, vol. 10, no. 5, p. 55112, 2013.

[50] D. R. Solli, G. Herink, B. Jalali, and C. Ropers, “Fluctuations and correlations in modulation instability,” *Nat. Photonics*, vol. 6, no. 7, pp. 463–468, Jun. 2012.

[51] B. Wetzel *et al.*, “Real-time full bandwidth measurement of spectral noise in supercontinuum generation,” *Sci. Rep.*, vol. 2, no. 1, p. 882, Dec. 2012.

[52] G. P. Agrawal, *Nonlinear Fiber Optics*. Academic Press, 2013.

[53] C. Rullière, *Femtosecond Laser Pulses: Principles and Experiments*. Springer Berlin Heidelberg, 2013.

[54] N. N. Akhmediev and V. I. Korneev, “Modulation instability and periodic solutions of the nonlinear Schrödinger equation,” *Theor. Math. Phys.*, vol. 69, no. 2, pp. 1089–1093, Nov. 1986.

[55] J. M. Dudley, F. Dias, M. Erkintalo, and G. Genty, “Instabilities, breathers and rogue waves in optics,” *Nat. Photonics*, vol. 8, no. 10, pp. 755–764, Sep. 2014.

[56] Q. Li, H. Zhang, X. Shen, H. Hao, and M. Gong, “Phenomenological model for spectral broadening of incoherent light in fibers via self-phase modulation and dispersion,” *J. Opt.*, vol. 18, no. 11, p. 115503, Nov. 2016.

[57] C. Finot, J. M. Dudley, B. Kibler, D. J. Richardson, and G. Millot, “Optical Parabolic Pulse Generation and Applications,” *IEEE J. Quantum Electron.*, vol. 45, no. 11, pp. 1482–1489, 2009.

[58] S. T. Sørensen, C. Larsen, U. Møller, P. M. Moselund, C. L. Thomsen, and O. Bang, “Influence of pump power and modulation instability gain spectrum on seeded supercontinuum and rogue wave generation,” *J. Opt. Soc. Am. B*, vol. 29, no. 10, p. 2875, Oct. 2012.

[59] K. Nithyanandan and K. Porsezian, “Influence of the functional form of nonlinearity in the Modulational Instability spectra of relaxing saturable nonlinear system,” *J. Phys. Conf. Ser.*, vol.

605, p. 12032, Apr. 2015.

[60] M. N. Islam, “Raman amplifiers for telecommunications,” *IEEE J. Sel. Top. Quantum Electron.*, vol. 8, no. 3, pp. 548–559, May 2002.

[61] P. T. Rakich, Y. Fink, and M. Soljačić, “Efficient mid-IR spectral generation via spontaneous fifth-order cascaded-Raman amplification in silica fibers,” *Opt. Lett.*, vol. 33, no. 15, pp. 1690–1692, Aug. 2008.

[62] Y. Wang, “Stimulated Raman scattering in high-power double-clad fiber lasers and power amplifiers,” *Opt. Eng.*, vol. 44, no. 11, pp. 114202–114212, 2005.

[63] J. Limpert, A. Liem, H. Zellmer, A. Tünnermann, S. Knoke, and H. E. D.-F. Voelckel M., Leonberger, F., Fujimoto, J., and Newton, S., “High-average-power Millijoule Fiber Amplifier System,” *Conf. Lasers Electro-Optics*, p. CThX3, 2002.

[64] Y. Wang, A. Martinez-Rios, and H. Po, “Experimental study of stimulated Brillouin and Raman scatterings in a Q-switched cladding-pumped fiber laser,” *Opt. Fiber Technol.*, vol. 10, no. 2, pp. 201–214, 2004.

[65] M. Melo, J. M. Sousa, and M. O. Berendt, “Stimulated Raman scattering mitigation through amplified spontaneous emission simultaneous seeding on high power double-clad fiber pulse amplifiers,” vol. 7914, p. 79142N, Feb. 2011.

[66] A. a Fotiadi and P. Mégret, “Self-Q-switched Er-Brillouin fiber source with extra-cavity generation of a Raman supercontinuum in a dispersion-shifted fiber.,” *Opt. Lett.*, vol. 31, no. 11, pp. 1621–1623, 2006.

[67] M. N. Zervas and C. A. Codemard, “High Power Fiber Lasers: A Review,” *IEEE J. Sel. Top. Quantum Electron.*, vol. 20, no. 5, pp. 219–241, Sep. 2014.

[68] R. Stolen and A. Johnson, “The effect of pulse walkoff on stimulated Raman scattering in fibers,” *IEEE J. Quantum Electron.*, vol. 22, no. 11, pp. 2154–2160, Nov. 1986.

[69] J. Limpert *et al.*, “High-average-power femtosecond fiber chirped-pulse amplification system.,” *Opt. Lett.*, vol. 28, no. 20, pp. 1984–6, 2003.

[70] A. Flores-Rosas, E. A. Kuzin, B. Ibarra-Escamilla, and J. M. Merlo-Ramírez, “The on-off contrast in an all optical switch based on stimulated Raman scattering in optical fibers,” *Laser Phys.*, vol. 22, no. 8, pp. 1340–1346, 2012.

[71] E. A. Kuzin, S. Mendoza-Vazquez, J. Gutierrez-Gutierrez, B. Ibarra-Escamilla, J. W. Haus, and R. Rojas-Laguna, “Intra-pulse Raman frequency shift versus conventional Stokes generation of diode laser pulses in optical fibers,” *Opt. Express*, vol. 13, no. 9, pp. 3388–3396, 2005.

[72] R. R. Alfano, *The Supercontinuum Laser Source: The Ultimate White Light*, 3rd ed. Springer New York, 2016.

[73] M. N. Islam, G. Sucha, I. Bar-Joseph, M. Wegener, J. P. Gordon, and D. S. Chemla, “Femtosecond distributed soliton spectrum in fibers,” *J. Opt. Soc. Am. B*, vol. 6, no. 6, p. 1149,

Jun. 1989.

[74] M. H. Frosz, O. Bang, and A. Bjarklev, “Soliton collision and Raman gain regimes in continuous-wave pumped supercontinuum generation,” *Opt. Express*, vol. 14, no. 20, p. 9391, Oct. 2006.

[75] F. Luan, D. V Skryabin, A. V Yulin, and J. C. Knight, “Energy exchange between colliding solitons in photonic crystal fibers,” *Opt. Express*, vol. 14, no. 21, pp. 9844–9853, 2006.

[76] L. Escalante-Zarate, Y. O. Barmenkov, S. A. Kolpakov, J. L. Cruz, and M. V Andrés, “Smart Q-switching for single-pulse generation in an erbium-doped fiber laser,” *Opt. Express*, vol. 20, no. 4, p. 4397, 2012.

[77] P. H. Reddy *et al.*, “Fabrication of Ultra-High Numerical Aperture GeO2 doped Fiber and Its Use for Broadband Supercontinuum Generation [in press],” *Appl. Opt.*

[78] J. del Valle-Hernandez, Y. O. Barmenkov, S. A. Kolpakov, J. L. Cruz, and M. V. Andres, “A distributed model for continuous-wave erbium-doped fiber laser,” *Opt. Commun.*, vol. 284, no. 22, pp. 5342–5347, 2011.

List of Publications

The following publications form the basis of the present thesis:

1. **Minguela-Gallardo, J. A.**, Barmenkov, Y. O., Kiryanov, A. V., Villegas-Garcia, I. L., Beltran-Perez, G., & Kuzin, E. A. "Spectral dynamics of actively Q-switched erbium-doped fiber lasers". *IEEE Photonics Technology Letters*, *29*(8), 683–686, 2017.

2. **Minguela-Gallardo, J. A.**, Barmenkov, Y. O., Kir'yanov, A. V., & Beltrán-Pérez, G., "Photon statistics of actively Q-switched erbium-doped fiber laser". *Journal of the Optical Society of America B*, *34*(7), 1407–1414, 2017.

Other publications

Barmenkov, Y. O., **Minguela-Gallardo, J. A.**, & Kiryanov, A. V. "Spectral and Noise Behaviors in Actively Q-Switched Erbium-Doped Fiber Laser" in Fiber Lasers: Advances in Research and Applications (1st ed., pp. 63–82). New York: Nova Science Publishers, Inc., 2017.

Pottiez, O., Bracamontes-Rodriguez, Y. E., Ibarra-Villalon, H. E., Garcia Sanchez, E., Lauterio-Cruz, J. P., Santiago-Hernandez, H., **Minguela-Gallardo, J. A.**, Hernandez-Garcia, J. C., Bello-Jimenez, M., Iballa-Escamilla, B., Hernandez-Garcia, J. C., Bello-Jimenez, M., & Kuzin, E. A. "Noise-Like Pulsing and Non-Stationary Operation of Passively Mode-Locked Fiber Lasers: Recent Advances and Applications" in Fiber Lasers: Advances in Research and Applications (1st ed., pp. 27–81). New York: Nova Science Publishers, Inc., 2017.

Harshavardhan, R. P., Kir'yanov, A. V., Dhar, A., Das, S., Dutta, D., Pal, Barmenkov Y. O., **Minguela-Gallardo, J. A.**, Bhadra, S. K., & Paul, M. C. "Fabrication of Ultra-High Numerical Aperture GeO2 doped Fiber and Its Use for Broadband Supercontinuum Generation". *Appl. Opt*. *56*(33), pp. 9315-9324, 2017.

Pottiez, O., Ibarra-Villalon, H. E., Bracamontes-Rodriguez, Y. E., **Minguela-Gallardo, J. A.**, Garcia-Sanchez, E., Lauterio-Cruz, J. P., & Kuzin, E. A. "Soliton formation from a noise-like pulse during extreme events in a fibre ring laser". *Laser Physics Letters, 14*(10), 105101, 2017.